Article

Geotechnical Characterization of Quito's North-Central Zone as Applied to Deep Excavation in the Urban Setting

Vicente E. Capa [1,*], F. Javier Torrijo [2,3], Pedro A. Calderón [1] and Carlos Hidalgo Signes [2]

1   Department of Construction Engineering, Universitat Politècnica de València, 46022 Valencia, Spain
2   Department of Geotechnical and Geological Engineering, Universitat Politècnica de València, 46022 Valencia, Spain
3   Research Centre PEGASO, Universitat Politècnica de València, 46022 Valencia, Spain
*   Correspondence: vcapa@cimentest.com or vicente_capa@hotmail.com; Tel.: +593-994-107-262

Abstract: This paper describes an in-depth soil characterization study in the La Carolina financial district of Quito (Ecuador). As there was very little information available on the geotechnical structure of Quito's volcanic soil, particularly in this area, where large-scale property development has taken place, the aim was to provide information on soil parameters to engineers working on large geotechnical and civil engineering projects based on the results of a thorough and comprehensive study of such properties. A series of field tests were performed at three different sites, where thin-walled tube samples were collected for lab testing to estimate the index properties and mechanical parameters. These index properties were then combined with conventional two-way drainage oedometer tests and stress-path triaxial testing to evaluate compressibility, stiffness and strength. The subsoil was found to be partly composed of slightly overconsolidated volcanic soils. X-ray Diffraction (XRD) and Scanning Electron Microscopy (SEM) analyses were also conducted to determine mineralogical and microstructural features and evaluate their influence on the mechanical behavior of the volcanic soil. This type of research is frequently applied to the study of landslides in urban environments, where it is essential to understand their failure mechanisms, especially in slopes generated by the construction of important engineering works. Therefore, based on this geotechnical characterization study, parameters were subsequently determined for the Mohr–Coulomb (MC), Hardening Soil (HS), and Hardening Soil with Small-Strain Stiffness (HSsmall) soil constitutive models, and these were applied to a numerical study of the Soil Nailing system behavior for the construction of a five-level underground car parking structure of an important building located in the north-central sector of the city of Quito. It was verified that the HSsmall and HS constitutive soil models better reproduce the behavior of this type of structure. Finally, the multiple geotechnical parameters determined in this study significantly contribute to the analysis of these structures in this soil type.

Keywords: in situ testing; laboratory tests; index properties; strength properties; underground car parking; soil nailing

1. Introduction

Quito is in the Guayllabamba river basin at the foothills of the Pichincha volcano in northern Ecuador. The aim of this experimental study was to evaluate the geotechnical soil characteristics in the La Carolina district (Figure 1) based on the results of routine and advanced lab and field tests. As few studies of this nature have been conducted in the city, a thorough study of the soils in this district could prove to be of great assistance to engineers and city planners.
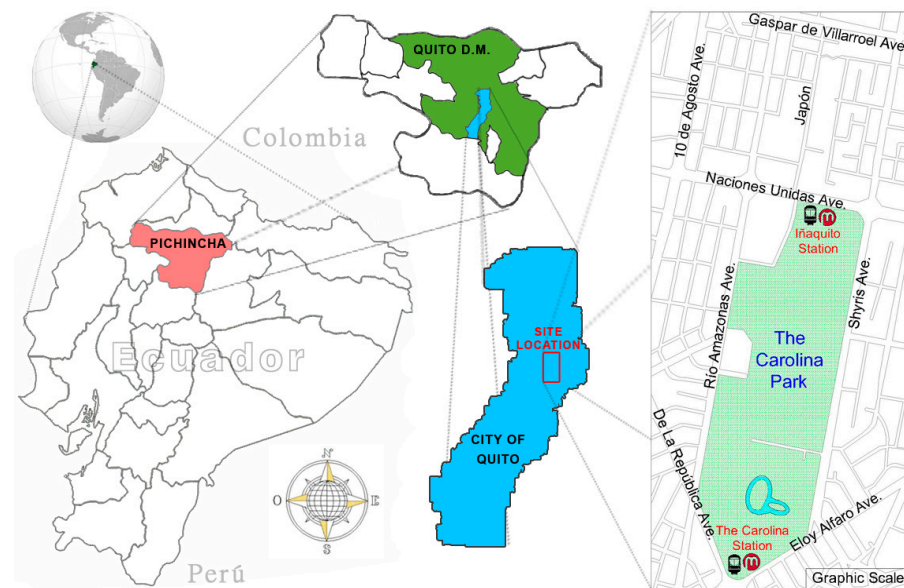
Figure 1. Map of Ecuador showing Quito, its capital, and the La Carolina sector.

The north-central zone of the city of Quito is characterized by moderate-to-large streets and avenues, with tall modern buildings and multi-story underground car parks, and thus, it was considered essential to carry out an extensive geotechnical study given the sparse amount of available information.

The subsoil in the zone object of this study comprises volcanic soils. As background information, Ecuador is a country with a great deal of volcanic activity and many volcanoes; however, very few complete studies have been carried out to characterize these types of materials [1]. For example, O'Rourke and Crespo [2] studied the volcanic soils in the eastern zone of the city of Quito; Belloni and Morris [3] studied the behavior of volcanic debris soils as they relate to slope stability in the El Reventador Volcano zone, located some 100 km northeast of the city of Quito, in the northern zone of eastern Ecuador, and Vezzoli et al. [4] performed a characterization study of the pyroclastic deposits from the Cotopaxi Volcano, which is located some 75 km southeast of the city of Quito. In the northern Andes, the Ecuadorian arc features a significant number of Quaternary volcanoes distributed in a relatively confined area [5]. Therefore, research groups such as Santamaria et al. [6], Andrade et al. [7], and Nauret et al. [8] have investigated important volcanoes in the central and northern regions of the Ecuadorian territory.

Volcanic soils constitute one of the most widely distributed groups in the world, especially in the Central and South American zones, Pacific Ocean islands, and the Caribbean, Africa, and Indonesia [9]. Thus, authors such as Bommer et al. [9], Crosta et al. [10], Gonzalez de Vallejo et al. [11], del Potro and Hürlimann [12], and Brandes and Nakayama [13] have presented various detailed surveys on volcanic soils at the international level, in which they present the different characteristics of these soils, focusing mainly on their basic properties, soil classification, compression and strength properties. However, studies carried out by researchers such as Hürlimann et al. [14], Moon et al. [15], Avşar et al. [16], and Okewale and Coop [17], in addition to the abovementioned properties, also include mineralogy and microstructure analyses. Some of the abovementioned studies are consistent in that volcanic soils mainly characterized by their high porosity and low bulk density were predominantly made up of silts and sands. Other studies are also in agreement for lightly cemented volcanic soils, such as the surveys by Yamanouchi and Murata [18] in their study of Japan's volcanic soils.

This study was carried out at three boreholes strategically distributed throughout the area that coincide with the construction of important building projects, designated as AMA1 (Río Amazonas Avenue), JAP1 (Japón Street), and AUS1 (Austria Street), using the Standard Penetration Test (SPT) to measure each meter of depth to a depth of 25 m.

The locations of the three boreholes are shown in Figure 2. The lab tests carried out at the Geotechnical Engineering Laboratory of the Universitat Politècnica de València (Spain) on disturbed and undisturbed samples from boreholes AMA1, JAP1, and AUS1 (which were stored in the laboratory's humidity chamber at a constant relative humidity of 100%) were based on four main characteristics: the index, compression, and strength properties, as well as deformation parameters under deviatoric loading.
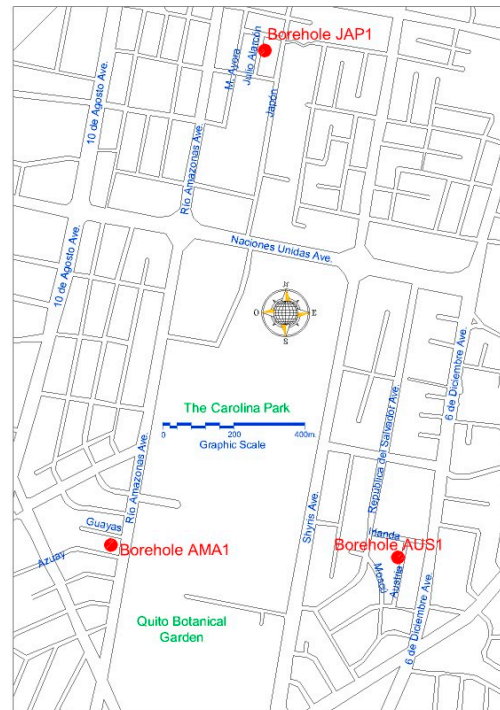

Figure 2. Locations of the three boreholes.

Furthermore, as part of this study, X-ray Diffraction (XRD) and Scanning Electron Microscopy (SEM) analyses were conducted to obtain the mineralogical and microstructural characteristics and obtain further parameters to compare with the volcanic soil studies carried out by other researchers.

Comprehensive geotechnical characterization studies are applicable to the investigation of landslides in urban environments in their different phases of analysis, design, monitoring, or landslide prevention. These natural (geological) or anthropogenic disasters demand specialized studies. Among the geological factors that can be mentioned are the presence of incompetent lithology, fault zones, slopes with high critical angles, and seismic activity. In terms of anthropogenic factors, there are modifications of slope gradients, constructions on slopes, and vibrations produced by heavy traffic [19]. Furthermore, a combination of factors, such as dense urban development, mountainous terrain, and intense seasonal rainfall, has led to serious landslide issues [20]. However, slope failure mainly occurs during heavy rainfall events when slow-moving regressive landslides turn into earth flows and mudflows [21].

Human activities are often responsible for inducing landslides in populated areas [22–25]. Excavation-induced landslides are typically observed in mining areas, particularly in sectors where hydrogeological conditions contribute to slope instability. However, such landslides are particularly prevalent in urban environments where human activities involve construction work, with or without excavation. Landslides often follow unplanned excavations, but uncontrolled loading resulting from any type of construction work in the upper part of a slope may also trigger a landslide. Additionally, new human settlements frequently necessitate urban and industrial development in steeply sloping mountainous regions, rendering these areas vulnerable and increasing the likelihood of landslides.

The stability of a slope resulting from excavation has always been a contentious issue. According to Burland et al. [26], Tsidzi [27], Bozzano et al. [28], Erginal et al. [23], and Zhang et al. [25], slope failure is caused by the release of induced stresses due to excavation. Many studies have demonstrated that geological and geotechnical investigations are essential to comprehend the failure mechanism of an earth structure, which will enable the creation of an appropriate geological model in numerical simulations [25]. Due to congested urban environments, current deep excavations are complex and require more specialized analyses to meet the needs of all stakeholders [29]. On the other hand, insufficient geotechnical and geological investigations and the inadequate interpretation of ground conditions often lead to slope failure and the subsequent costs of repair work [30]. All of the above clearly justifies the need for a comprehensive geotechnical characterization study for landslide analysis and evaluation.

Throughout history and across the globe, numerous landslides induced by prior human activities have been identified. In Busan (South Korea) in the late 1990s, cut slopes were created on a hillside to provide space for housing and industry. However, later analyses revealed that the original investigations, designs, and subsequent studies were inadequate, resulting in the slope failing six times despite nine reassessment surveys and the implementation of various remediation alternatives over a 7-year period until a catastrophic collapse occurred in 2002 [30].

In contrast, in Praia de Boa Viagem (Brazil) in 2003, a 31-meter excavation was carried out to construct a building. To ensure stability, two levels of anchored walls were planned. However, when the upper wall was nearly completed, a crack appeared at its top, prompting a halt to construction for further investigation [31]. These studies revealed the presence of clay minerals with high activity and low shear strength that were not identified in the initial study. Consequently, the walls were reinforced with additional anchors, and a Soil Nailing system was incorporated. During and after the construction, the excavation was monitored using load tests on the anchors, inclinometers to control horizontal ground deformations, and an electronic distance-measuring device to monitor horizontal and vertical ground surface and wall movements. Strain Gauges were also installed on the steel bars to monitor their tension.

In March 2011, a landslide took place on a slope around 18.3 m in height in Santa Clara, California (USA), and according to specialized studies conducted afterward, it was found that the landslide was induced by a significant cut made in the terrain along the bottom of the slope between 2000 and 2004 [32]. Before the landslide, a residential structure had been constructed near the slope's base.

On the other hand, given the involvement of anthropogenic factors, the construction of geotechnical engineering works commonly generates risks that require special attention. Thus, in the construction of most underground building structures in the Ecuadorian capital, the Soil Nailing technique is frequently applied during the excavation process as a method for reinforcing the ground during the excavation process, with some variations according to the equipment available in the region and the specifications of each project. However, this technique, which has proved to be effective for the management of soil excavations in the city of Quito, currently lacks local research, whether theoretical, numerical, or experimental, based on the geotechnical properties of the volcanic soils that characterize the area [1].

The Soil Nailing technique has been successfully applied globally to slope stabilization in several geotechnical engineering projects in countries such as the United States [33], Chile [34], China [35], Ireland [36], and Brazil [31], among others. Similarly, several numerical studies of the behavior of this type of structure have been carried out, such as those presented by Fan and Luo [37], Singh and Sivakumar Babu [38], Wei and Cheng [39], Rabie [40], Rawat and Gupta [41], Bayat et al. [42], and Capa et al. [43], among others. These investigations have verified the technique's high degree of efficiency in its practical application and are supported by important numerical analyses.

In view of the above and as an application to the geotechnical characterization study, a numerical analysis is presented using the finite element method with PLAXIS 2D [44,45]

of a typical Soil Nailing structure for the construction of a building with 5 underground parking levels (h = 15.5 m) and 15 stories in height. This building was constructed from 2017 to 2020 and is located precisely in the area of the JAP1 borehole (Figure 2), in the north-central area of the city of Quito. For the analysis with PLAXIS 2D [44–46], the Mohr–Coulomb (MC), Hardening Soil (HS), and Hardening Soil with Small-Strain Stiffness (HSsmall) soil constitutive models were considered. This analysis focuses primarily on the evolution of tensile forces in the anchor bars and the analysis of horizontal displacements of the facing and settlements in the soil induced by basement-level construction. This research additionally includes an analysis of the factors of safety (FoSs) established during the different construction phases and carried out by means of limit equilibrium methods and the finite element method.

The analysis of all the aforementioned variables is crucial in the stability study of ground reinforcement structures applied in the field of urban excavations in civil construction works. Naturally, having comprehensive geotechnical characterization studies also allows for the creation of numerical models that more accurately reflect reality.

2. Geological Setting

The Ecuadorian Andes mountain range covers an area of approximately 650 km by 150 km [47], which crosses Ecuador from the south to the north, predominately in the NNE–SSW direction [48]. This mountain chain began to develop at the end of the Cretaceous period as a result of the subduction movements of the Nazca Plate and the Carnegie Ridge (an underwater mountain ridge situated on the Nazca Plate) under the South American plate, generating a compressive tectonic regime dominating from E-W up until present times [47–49] (Figure 3). The Carnegie Ridge is emerging in the active Galapagos hotspot [50].

In Ecuador, the volcanic arc related to the subduction of the Nazca Plate has a width of 120 km and is divided into three regions: the forearc, extending along the Western Range or Cordillera Occidental; the main arc, situated in the Eastern Range or Cordillera Real; and the back-arc, located in the upper Amazon regions. The volcanoes in the forearc (Pululahua, Atacazo, Illiniza, Quilotoa, and the Pichincha Volcanic Complex) are mainly dacitic centers, whereas those in the main and back-arc (Antisana, Cotopaxi, Tungurahua, Sangay, and El Reventador) are mainly andesitic in composition [51]. The Inter-Andean Depression, which has been evolving since the Miocene epoch [52,53], is located between the Western Range and the Eastern Range. During the development of the Inter-Andean Depression, tectonic rearrangements of the Late Miocene progressively led to the formation of various basins that were filled with alluvial, fluvial, lacustrine, and volcanic deposits, including the Quito Basin [54].

The urban area of Quito is situated within the Quito Basin, oriented in a north–south direction. The study area is positioned to the east of the Pichincha Volcanic Complex. The Quito Basin's eastern boundary is defined by an actively moving reverse fault that dips toward the west [55]. The curved geometry of this fault is likely a consequence of the Pichincha Volcanic Complex's propagation [51].

In terms of stratigraphy, the area of interest (north-central Quito) corresponds to recent deposits that rest on the Cangahua Formation (tufa and volcanic ash from the Quaternary period). The northern, southern, and eastern zones of the area of interest are stratigraphically characterized by lacustrine fluvial sedimentary deposits [56] with clearly defined stratified layers of sandy silts and dark brown, light brown, and yellowish-gray sands, with some pumice lapilli. Decomposed organic matter is present in most of the surface layers. The western zone consists of a colluvial deposit [56] with no clear deposition sequence and generally consists of materials of varied granulometric size, including gravel and boulders.
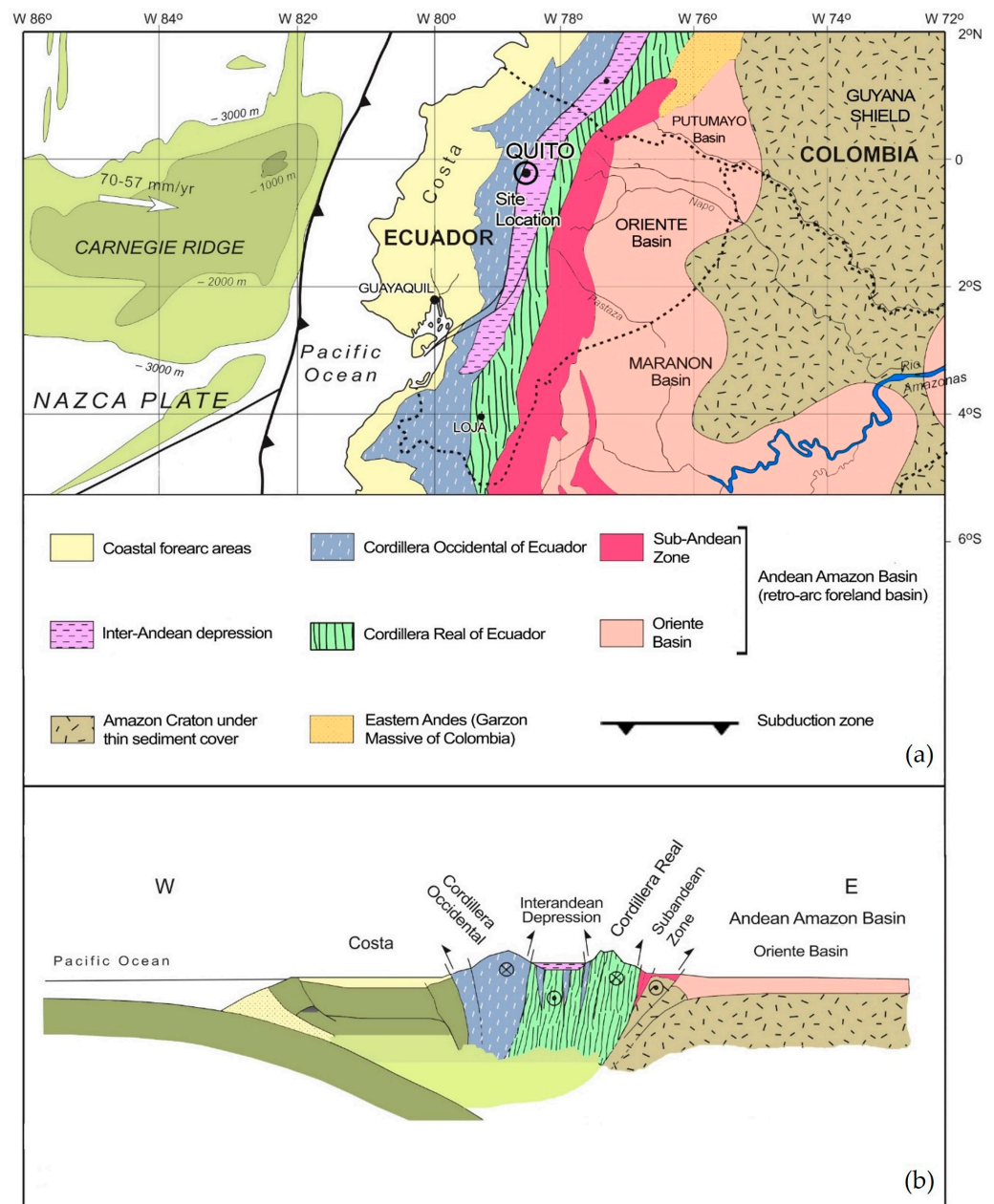
Figure 3. (**a**) Tectonic Map of Ecuador; (**b**) schematic tectonic cross-section toward the north of Ecuador. Modified from [57,58].

On the other hand, the geological and geotechnical study for Line 1 of the Quito Metro [59] indicated the presence of surface fill soils in several areas of La Carolina. However, in the three drillings carried out during this study and located relatively close to the Quito Metro study, we did not detect any such materials.

3. Geotechnical Characterization Study

3.1. In Situ Testing and Soil Samples

3.1.1. Standard Penetration Test

The most widely used and cost-effective in situ test to obtain subsurface information is the Standard Penetration Test (SPT), which measures soil resistance to penetration at any given depth. It can also be used to estimate the properties of granular soils [60], correlate the undrained shear strength of cohesive soils, and calculate the soil-bearing capacity and settlement. In this study, the SPT was carried out in accordance with the ASTM D1586

standard [61]. Figure 4a shows the penetration depth plotted against the number of blows (N_{SPT}) obtained for the penetration resistance test in boreholes JAP1, AMA1, and AUS1.
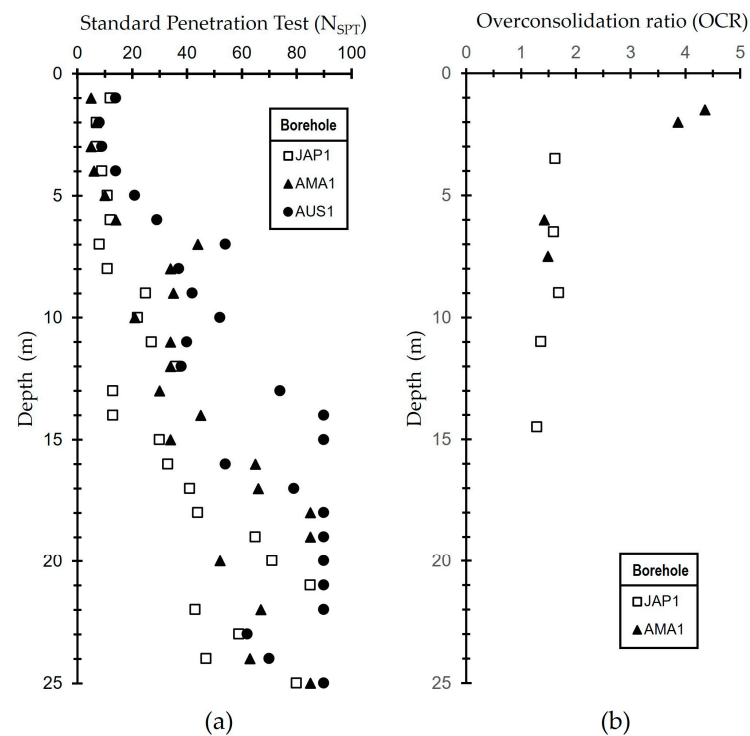

Figure 4. (**a**) SPT log profiles of boreholes JAP1, AMA1, and AUS1; (**b**) overconsolidation ratios of boreholes JAP1 and AMA1.

Furthermore, the preconsolidation stress was estimated by oedometer testing. Figure 4b shows the corresponding overconsolidation ratios (OCRs). The values range from 1.62 at a depth of 3.5 m to 1.30 at 14.5 m.

3.1.2. Soil Sampling

A geotechnical site investigation is the process of soil characterization, which requires undisturbed high-quality samples. Tube sampling is the easiest and most cost-effective manner of sampling, although it has been associated with sample disturbance. In this study, 600 mm × 78 mm diameter stainless-steel tubes and a wall thickness of t = 1.50 mm were used to collect samples from boreholes JAP1 and AMA1. The ratio of the external diameter to wall thickness, De/t, was 50.7, which is higher than the minimum De/t recommended by Ladd and DeGroot [62].

3.2. Index Properties and Soil Composition

All sample testing was carried out in accordance with ASTM [63] and UNE [64] standards. This section provides the index properties and soil composition data obtained from the tests.

3.2.1. Natural Water Content and Atterberg Limits

Variation values of the natural water content (w_{nat}), liquid limit (LL), and plastic limit (PL) are shown in Figure 5a–c. The depth profile of natural water content in borehole JAP1 ranged from 13% to 50% and decreased normally with depth to 16 m. In AMA1, a uniform range of values was found from 12% to 26%, while in AUS1, the natural water content distribution was between 9% and 33%. The plastic limit (PL) ranged from 16 to 34 (average ~25), while the liquid limit (LL) values ranged from 18 to 64 (average ~35). Figure 5d shows the depth profile of the liquidity index (LI), which ranges from −2.0 to 1.0.
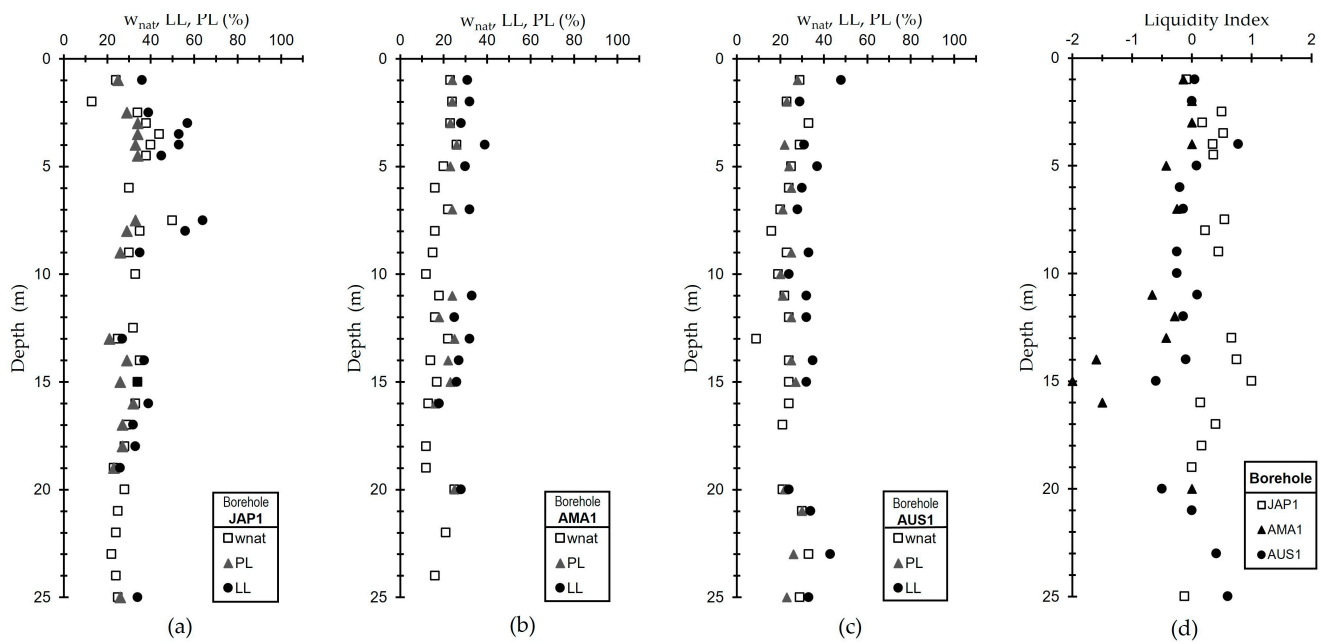
Figure 5. Natural water content, LL, and PL: (**a**) borehole JAP1; (**b**) borehole AMA1; (**c**) borehole AUS1; (**d**) liquidity index versus depth for boreholes JAP1, AMA1, and AUS1.

Figure 6 shows Casagrande plasticity charts for samples from boreholes JAP1, AMA1, and AUS1. It is evident that all the samples lie close to the A-line. Most of those from JAP1 are classified as silts and clays with low-to-high plasticity, while most from AMA1 and AUS1 are silts and clays with low-to-intermediate plasticity.
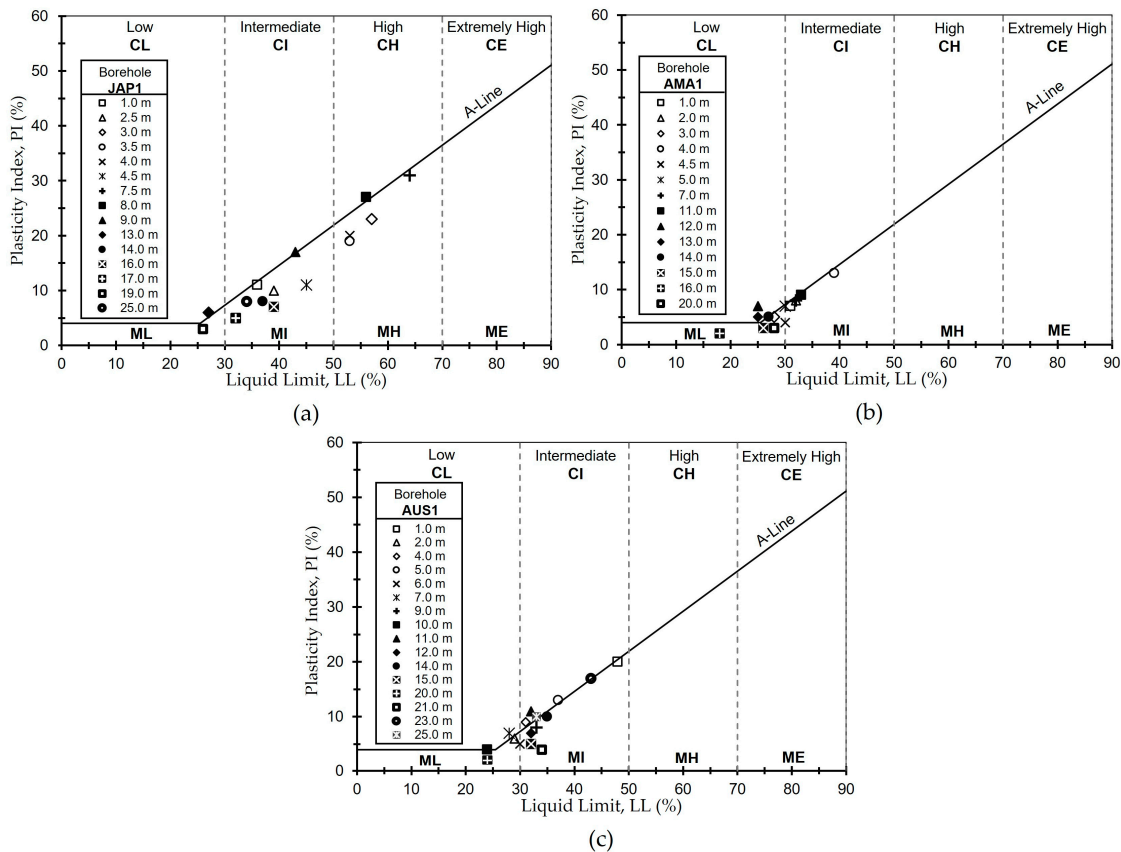

Figure 6. Soil plasticity of tested samples: (**a**) borehole JAP1; (**b**) borehole AMA1; (**c**) borehole AUS1.

3.2.2. Particle Size Distributions

Figure 7a shows the particle size distribution profiles for specimens from borehole JAP1. Silt content ranged from 37 to 64% (average ~53%) between depths of 1.0 m and 14.5 m, although sand content was predominant below the 14.5 m level, with maximum values up to 71%.
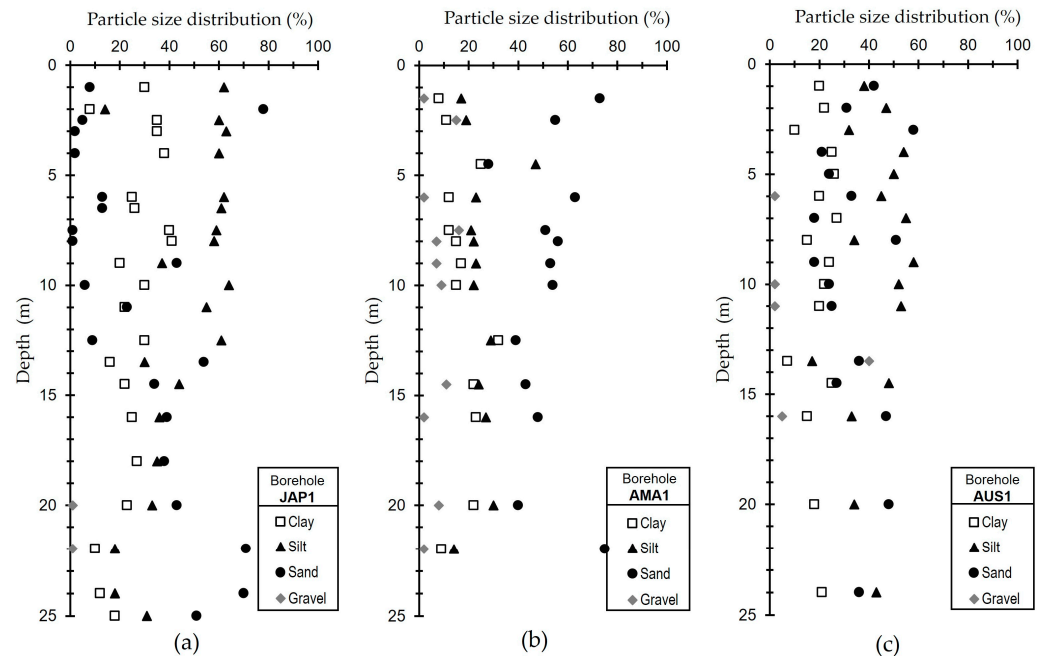

Figure 7. Particle size distributions: (**a**) borehole JAP1; (**b**) borehole AMA1; (**c**) borehole AUS1.

Figure 7b shows that the particle size distribution for samples from borehole AMA1 is fairly constant at all depths, and sand content ranged from 28% to 75% (average ~52%). Figure 7c shows the particle size distribution for specimens from borehole AUS1, in which fine content was predominant throughout (42% to 84%). According to the Unified Soil Classification System (USCS), these soils are classified as ML, MH, CL, CL-ML, and SM. By way of comparison, the volcanic soils from the eastern zone of the city of Quito studied by O'Rourke and Crespo [2] were found to consist of material containing approximately 60–65% fine sand and 10–15% clay by weight, with the remaining fraction being silt.

3.2.3. Specific Gravity and Bulk Density

The specific gravity values are reported in Figure 8a. In general, these values are between 2.35 and 2.65 in borehole JAP1. In AMA1 samples, these range from 2.61 to 2.70 and from 2.50 to 2.55 in AUS1. The studied soils presented low specific gravity values, in agreement with those found by O'Rourke and Crespo [2], Bommer et al. [9], Crosta et al. [10], and Avşar et al. [16].

Bulk density values are shown in Figure 8b. The values measured for samples range between 1.44 and 1.91 Mg/m^3 in JAP1, between 1.80 and 2.03 Mg/m^3 in AMA1, and between 1.62 and 1.73 Mg/m^3 in AUS1. Bulk density values were found to be low, as in O'Rourke and Crespo [2], Hürlimann et al. [14], Bommer et al. [9], Crosta et al. [10], and Avşar et al. [16].
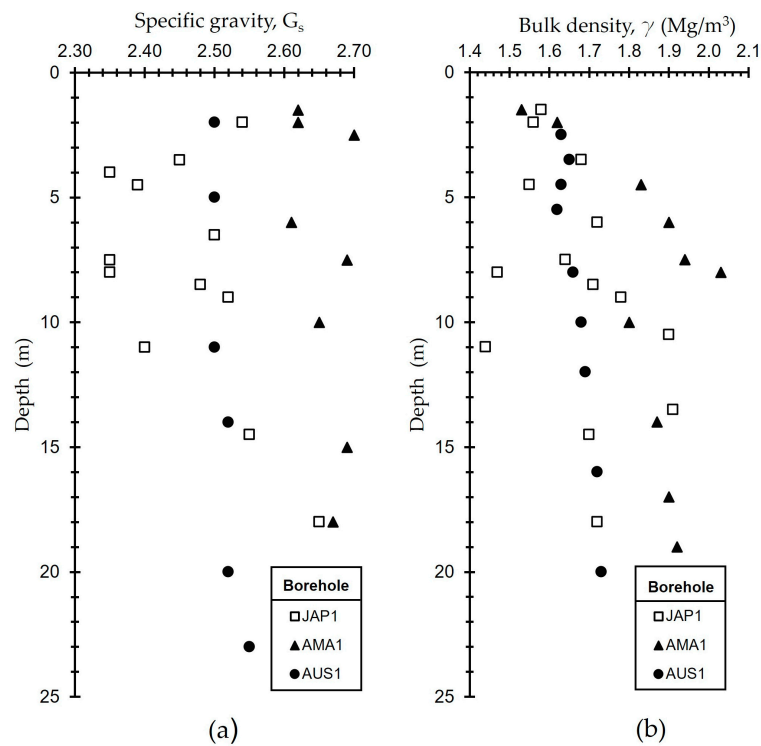
Figure 8. (**a**) Specific gravity versus depth of boreholes JAP1, AMA1, and AUS1; (**b**) bulk density versus depth of boreholes JAP1, AMA1, and AUS1.

3.2.4. Void Ratio and Porosity

Void ratio values are shown in Figure 9a. These vary between 0.88 and 1.92 in JAP1 and between 0.49 and 0.99 in AMA1. These void ratio values are within the range of those of the volcanic soils studied by O'Rourke and Crespo [2], Hürlimann et al. [14], and Bommer et al. [9].
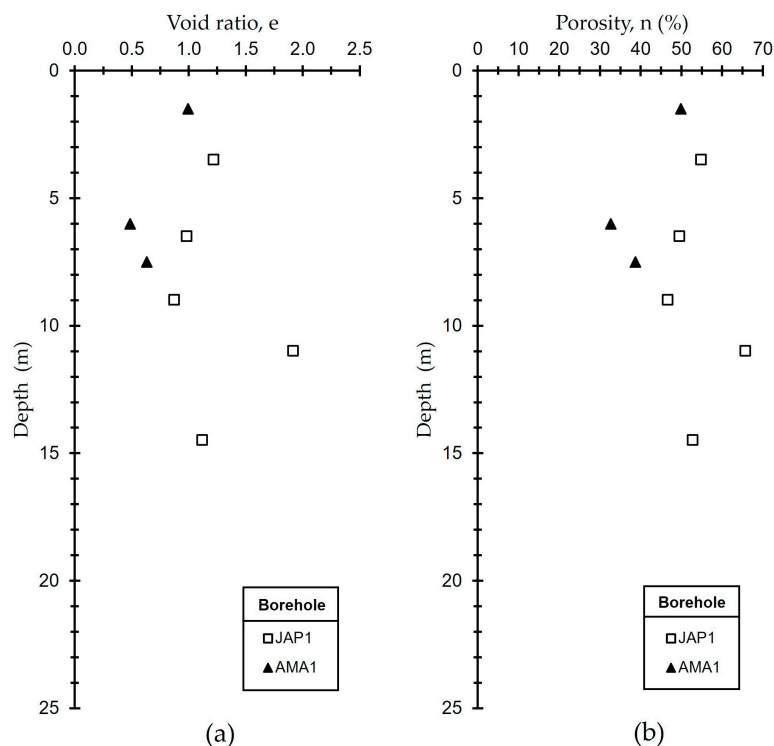

Figure 9. (**a**) Void ratio versus depth; (**b**) porosity versus depth for boreholes JAP1 and AMA1.

Figure 9b shows the porosity values, which were found to range between 47% and 66% in JAP1 and between 33% and 50% in AMA1. Likewise, the studied soils have high porosity values, in agreement with the volcanic soil studies by O'Rourke and Crespo [2], Hürlimann et al. [14], Bommer et al. [9], and Avşar et al. [16].

3.2.5. Carbonate Content and Organic Content

The Bernard Calcimeter method was used to determine the calcium carbonate content of the specimens obtained from boreholes JAP1 and AMA1. The carbonate content variation with depth is shown in Figure 10a. The values range from 4.0% to 5.7% for the samples from JAP1 and between 3.7% and 6.2% for the specimens from AMA1.
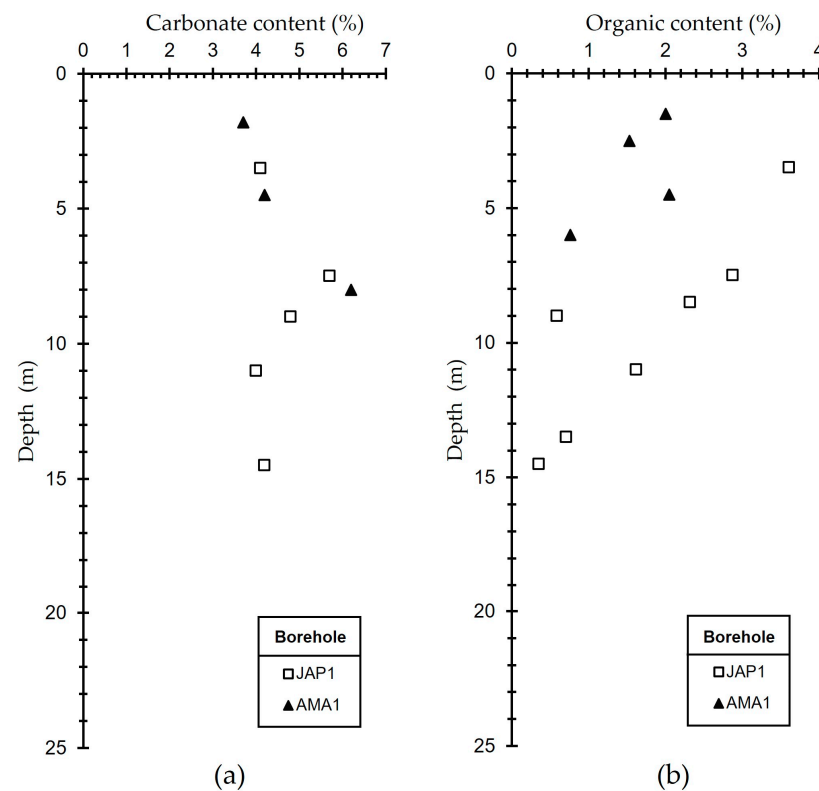

Figure 10. (**a**) Carbonate content versus depth for boreholes JAP1 and AMA1; (**b**) organic content versus depth for boreholes JAP1 and AMA1.

The potassium permanganate method was used to determine the organic content (OC) of samples from JAP1 and AMA1. Figure 10b shows the organic content variation with depth, which ranges between 0.35% and 3.61% for specimens from JAP1 and between 0.76% and 2.05% for those from AMA1. In both cases, the values show a clear tendency to decrease with depth.

3.2.6. Mineralogy

Quantitative X-ray Diffraction (XRD) analyses (Table S1) were performed on samples from JAP1 and AMA1 to determine the breakdown of soil mineral crystal structure parameters. Prior to XRD analysis, the samples were dried to remove moisture content and powdered until the grain could pass through an 80 μm sieve. The mineral composition of the soils was determined by XRD analysis on both randomly oriented powder and oriented aggregates [65]. The studied samples were composed of plagioclases (7.5–69.2%), pyroxenes (1.4–32.3%), amphiboles (7.0–27.9%), phyllosilicates (0.0–4.8%), inosilicates (0.6–4.6%), silica (0.9–9.5%), sulfides (1.1–2.6%), and carbonates (0.5–2.3%). Detailed results obtained from the quantitative analysis of the mineral data are provided in Figure 11.
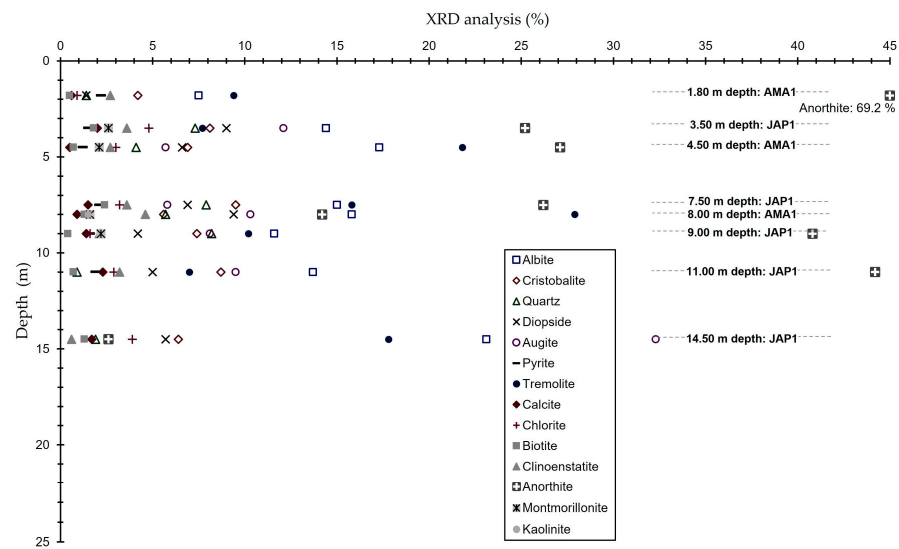
Figure 11. Quantitative X-ray Diffraction (XRD) analysis versus depth for samples JAP1 and AMA1.

3.2.7. Microstructure

Scanning Electron Microscopy (SEM) was performed with a Model JSM 6300 Scanning Microscope using intact oven-dried samples. Plagioclase, Augite, Tremolite, Diopside, and Cristobalite–Quartz are dominant in each sample, consistent with the values recorded in the mineralogical analysis (Mineralogy section). Figure 12 shows the microstructures of specimens from JAP1 and AMA1. Gas bubbles and organic matter can be identified in Figure 12b and could be the main reason for the low density values.
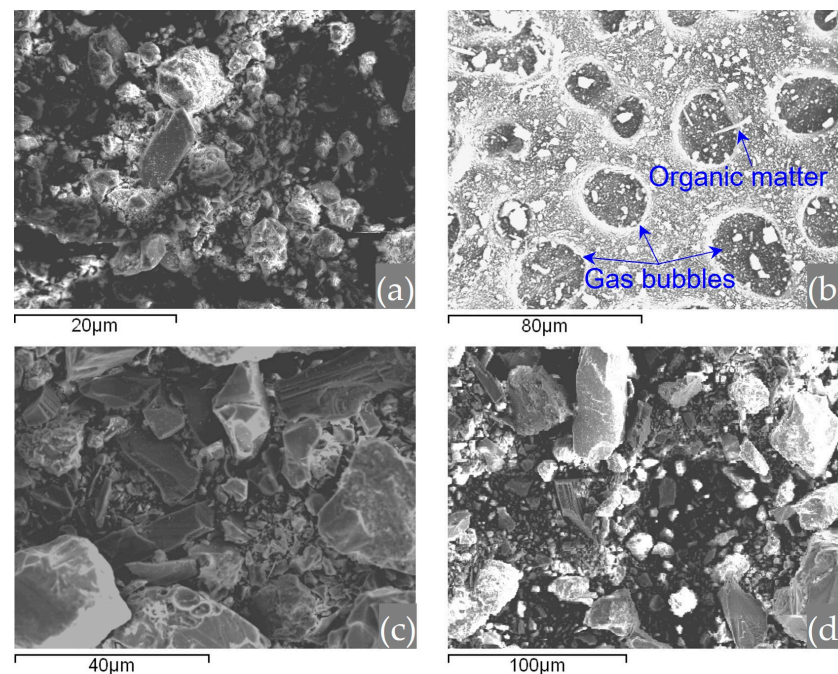
Figure 12. SEM micrographs showing soil samples: (**a**) 9 m depth in JAP1; (**b**) 11 m depth in JAP1; (**c**) 1.8 m depth in AMA1; (**d**) 8 m depth in AMA1.

3.3. Compression Properties

Conventional two-way drainage oedometer tests were carried out on undisturbed specimens to evaluate the soil compression parameters, in accordance with the ASTM D2435 standard [66]. The diameters of stainless-steel oedometric rings used were 45 mm, 50 mm, and 70 mm, with a height of 20 mm. Each load increment was maintained for 24 h.

Overburden stress was increased from 5 kPa to 1000 kPa, but some samples were loaded up to 2000 kPa.

It is common and frequent for these types of tests to be performed on samples of clayey strata. However, in this study, oedometric tests were carried out on samples comprising mostly sand, an uncommon situation that is nevertheless not incorrect. On the contrary, oedometric curves that can be applicable to the analysis of vertical deformations in terrain with volcanic soils consisting mostly of sand, under different load solicitations, were determined. In this study, all samples from borehole AMA1 were composed of silty sands.

To make the research more comprehensive, repetitive instances of "load-unload-reload-unload" states were performed on several samples, which required many days of analysis, considering that each load and unload step represents a day of testing. However, this allowed for verification that the unload curves are practically parallel in both unload instances.

Additionally, advanced soil constitutive models such as Hardening Soil (HS) and Hardening Soil with Small-Strain Stiffness (HSsmall) require the oedometric tangent modulus, which is precisely determined through these tests [46]. Therefore, a practical application that normally yields consistent and more reliable results is the analysis of Soil Nailing retaining structures with these soil constitutive models. These structures are common in the control of landslides in urban environments and often have multilayer strata with variations of fine soils and sandy soils, and thus, conducting such oedometric tests on sandy soils is clearly justified.

Figure 13 shows typical one-dimensional compression oedometer test results for samples from boreholes JAP1 and AMA1 in terms of the effective stress and the corresponding void ratio.
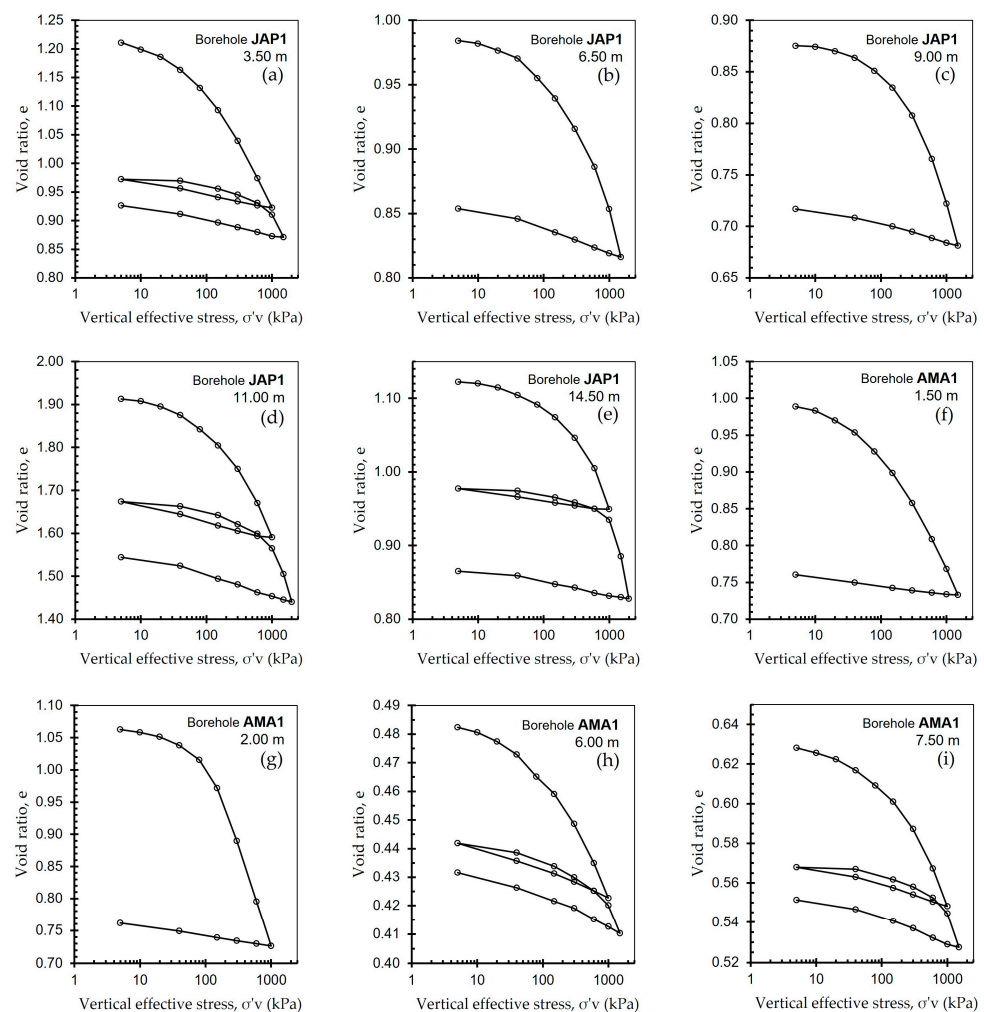

Figure 13. One-dimensional compression oedometer tests of samples from JAP1 and AMA1.

For the JAP1 borehole, the compression index (C_c) sample values range between 0.15 and 0.36, and the swelling index (C_s) values are in the range of 0.02 to 0.05. AMA1 has C_c values between 0.06 and 0.30 and C_s values between 0.01 and 0.02.

Figure 14a shows the relationship between the compression index (C_c) and the natural moisture content (w_{nat}) and liquid limit (LL) for soils from JAP1 and AMA1. Figure 14b shows the correlation between the swelling index (C_s) and the natural moisture content (w_{nat}) and liquid limit (LL). Figure 14c shows the relationship between compression (C_c) and swelling indexes (C_s) versus initial void ratios (e_0). C_c generally presents a good correlation with e_0 or w_{nat} for most clay types [67].
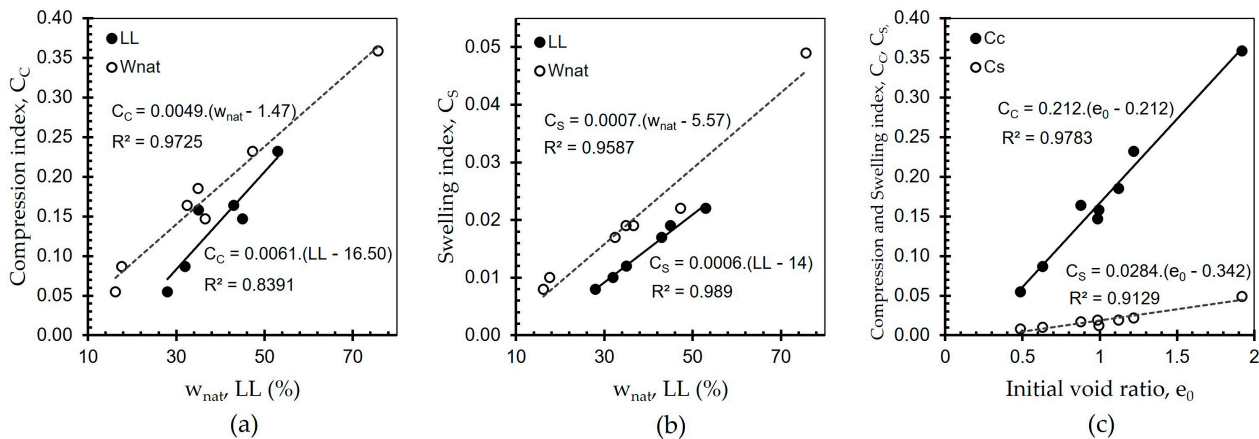

Figure 14. Correlation between (**a**) compression index (C_c) and (**b**) swelling index (C_s) with the natural moisture content (w_{nat}) and liquid limit (LL); (**c**) correlation between compression (C_c) and swelling (C_s) indexes with Initial void ratios (e_0).

Empirical formulas are obtained for the soil of the study area, according to Figure 14.

$$C_c = 0.0049 \, (w_{nat} - 1.47) \tag{1}$$

$$C_c = 0.0061 \, (LL - 16.50) \tag{2}$$

$$C_c = 0.212 \, (e_0 - 0.212) \tag{3}$$

$$C_s = 0.0007 \, (w_{nat} - 5.57) \tag{4}$$

$$C_s = 0.0006 \, (LL - 14) \tag{5}$$

$$C_s = 0.0284 \, (e_0 - 0.342) \tag{6}$$

The ratio of C_c/C_s is a constant value and, in these cases, varies between 6 and 10.

3.4. Strength Properties

The shear strength of soil is its ability to resist failure and displacement between its particles when acted upon by an external force. This concept is fundamental when estimating the lateral soil pressure on retaining structures and in slope stability analysis.

In this study, consolidated-undrained triaxial tests (CU) and consolidated-drained triaxial tests (CD) were carried out in the hydraulic stress path cells of the Geotechnical Engineering Laboratory of the Universitat Politècnica de València. These analyses are the only ones to be performed to date in this specific region and should provide a valuable resource that will prove useful for future research.

3.4.1. Undrained Shear Strength Properties

The undrained soil shear strength plays a fundamental role in geotechnical engineering, providing important information to calculate the pressures exerted by soils in undrained conditions (short-term stability) and the bearing capacity, for example, in soils supporting gravity wall foundations. It is also an indicator of soil behavior, in association with other engineering properties.

In this study, consolidated-undrained (CU) triaxial compression tests with pore water pressure measurements were carried out in accordance with the ASTM D4767 standard [68]. A very fine wire saw was used to trim the specimens to a diameter of 38 mm and a height of 76 mm in a soil lathe. Each triaxial test comprised three different stages: (1) saturation, (2) consolidation, and (3) shearing under undrained conditions [69]. A stress-controlled saturation ramp was used until the point when the cell and back-water pressures reached 610 kPa and 600 kPa, respectively. These values were held for approximately 24 h, after which Skempton's parameter B was determined, finding the values to be higher than 0.96 in every instance. All the specimens followed isotropic consolidation, in which pore water drainage was provided at the top of the sample. At the same time, the excess pore water pressure was measured with a pore pressure transducer connected to the bottom drainage line. Each specimen was then subjected to undrained shearing, with an axial displacement rate equal to 0.03 mm/min.

The q-p' plane is used to represent the test results; thus, $p' = (\sigma'_1 + 2\sigma'_3)/3$ and $q = \sigma'_1 - \sigma'_3$, where σ'_1 is the stress applied to a test specimen in the vertical (axial) direction, and σ'_3 is the all-round pressure applied to a test specimen in the triaxial cell chamber.

Different failure criteria are used to determine the shear strength of a soil sample, including the peak deviator stress, maximum principal stress ratio, limiting strain, critical state, and residual stress. In this study, the maximum stress ratio σ'_1/σ'_3 criterion was adopted as a failure criterion, from which the soil's shear strength is determined. This ratio provides a better correlation of shear stress versus normal stress in Mohr stress circles at failure. The ratio is equal to 1 at the start of the test, because in this stage, $\sigma'_1 = \sigma'_3$. The maximum value of σ'_1/σ'_3 does not necessarily occur at the same strain as the peak deviator stress. Peak values of the stress ratio σ'_1/σ'_3 vary between 4.00 and 5.35, with the axial strain, ε_s, ranging from 3.75% to 6.00%, whereas the post-peak values of this stress ratio range from 3.55 to about 4.65. Figure 15a shows the variation in the stress ratio, σ'_1/σ'_3, with the axial strain, ε_s, for samples from boreholes JAP1 and AMA1. The variation in the stress ratio, q/p', with the axial strain, ε_s, is shown in Figure 15b. In this case, the post-peak values of the stress ratio vary between 1.35 and 1.65.
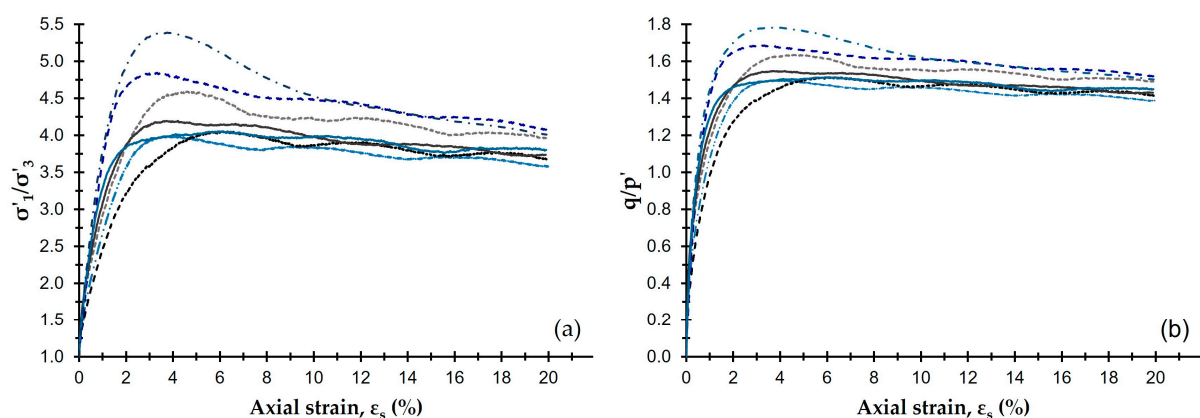
Figure 15. (**a**) Stress ratio σ'_1/σ'_3 variation for samples from boreholes JAP1 and AMA1; (**b**) stress ratio q/p' variation for samples from boreholes JAP1 and AMA1.

Figure 16 shows the stress–strain curves, q-ε_s, with the evolution of pore pressure (u), obtained for samples from boreholes JAP1 and AMA1.
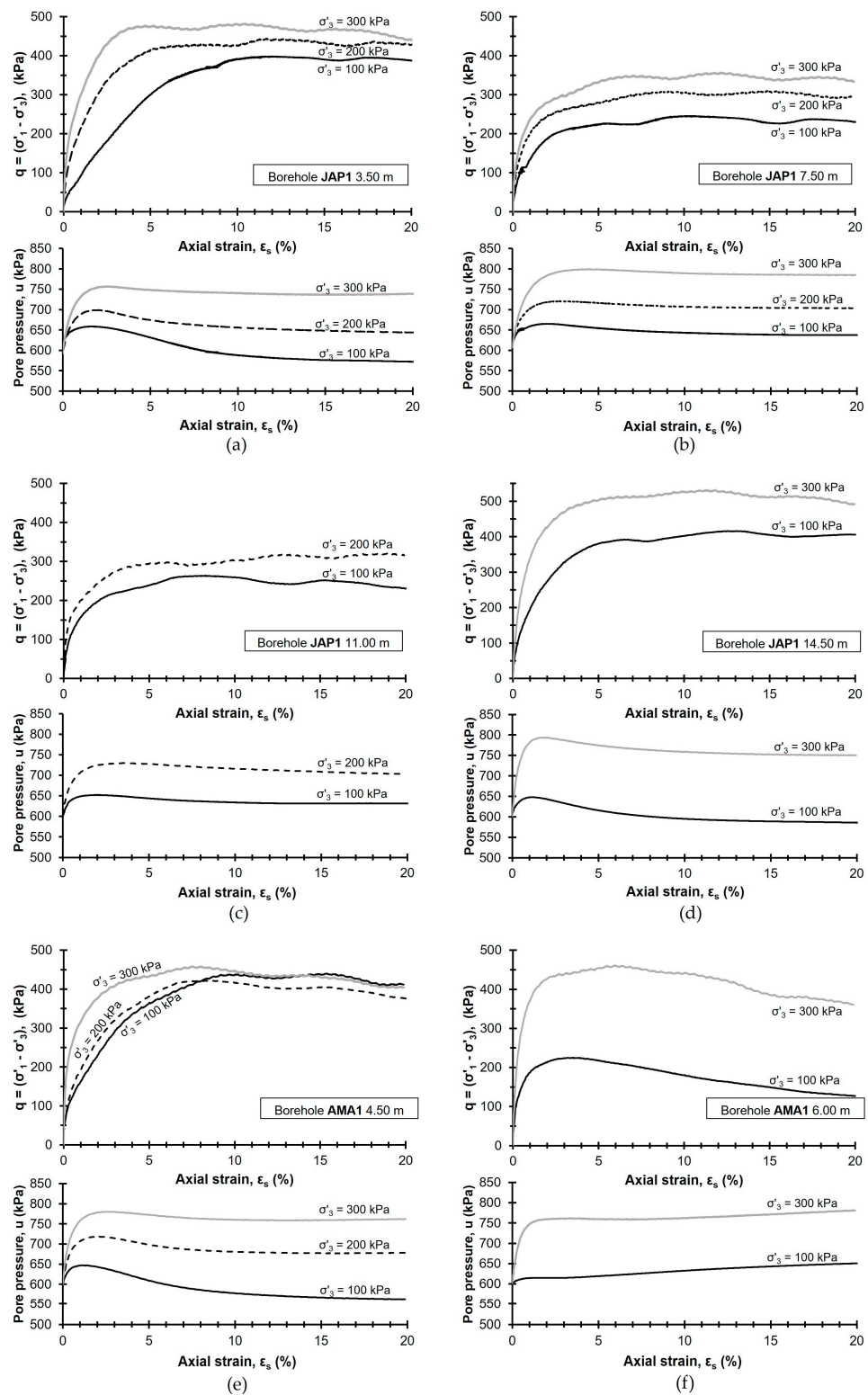
Figure 16. Stress–strain–pore-pressure curves for samples from boreholes JAP1 and AMA1.

The stress ratio q/p′ behavior was classified into two main groups, as seen in Figure 17, which shows that the undrained strength in compression was determined using the critical soil mechanics concept. The (M) slope of the critical state line in compression [70,71] is obtained by Equation (7).

$$M = \frac{6\sin\varnothing'}{3 - \sin\varnothing'} \tag{7}$$
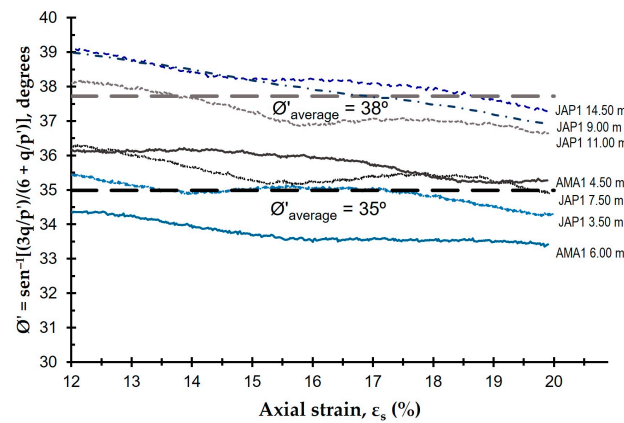
Figure 17. Secant effective friction angle ($\varnothing'$) for samples from boreholes JAP1 and AMA1.

The secant friction angle, $\varnothing'_{sec}$, was estimated for axial strains greater than 12%. Average friction angles of 35° (specimens from depths of 3.50 m to 7.50 m) and 38° (specimens from depths of 9.00 m to 14.50 m) constitute the post-peak response of samples from JAP1 and AMA1. This relationship between $\varnothing'_{sec}$ and sample depth, however, is not definitive, given that some factors (such as particle shape, size distribution and configuration, grain mineralogy, void ratio, water content, and previous stress history) can affect the soil strength measured in a lab test [72].

Figure 18 shows the stress paths in the q-p' plane for the samples from JAP1 and AMA1 under triaxial conditions. The soil behavior under shearing is easily observed in the effective stress paths shown in these figures. Peak friction angles between 34° and 38° were estimated in triaxial compression for these two borehole samples.

Figure 18. Effective stress paths: (**a**,**b**) samples from borehole JAP1; (**c**) samples from AMA1.

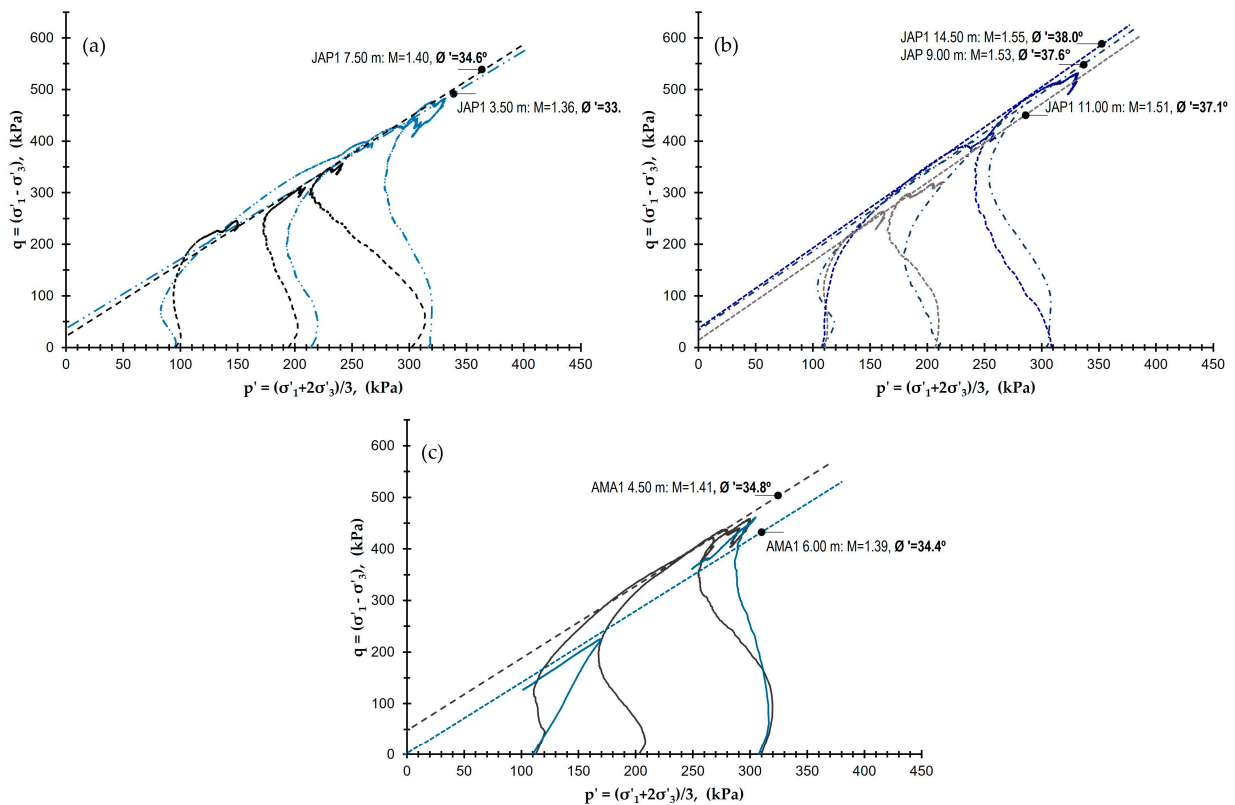A summary of the strength parameters obtained from the consolidated-undrained (CU) triaxial compression tests from JAP1 and AMA1 is provided in Table 1. The shallow specimens show a peak friction angle of $\varnothing'_{peak} \approx 35°$ and an effective cohesion (c′) between 5 kPa and 26 kPa, whereas the deep samples show a peak friction angle of $\varnothing'_{peak} \approx 38°$ and an effective cohesion (c′) between 10 kPa and 20 kPa.

Table 1. Undrained strength parameters for samples from boreholes JAP1 and AMA1.

Test Borehole	Depth (m)	Cell Pressure (kPa)	Triaxial Test	w_{nat} (%)	γ/γ_d [1] (kN/m^3)	c′ (kPa)	$\varnothing'$ (°)
JAP1	3.50	100, 200, 300	CU	43	16.8/11.7	21	33.7
AMA1	4.50	100, 200, 300	CU	25	18.3/14.6	26	34.8
AMA1	6.00	100, 300	CU	16	19.0/16.4	5	34.4
JAP1	7.50	100, 200, 300	CU	50	16.4/10.9	14	34.6
JAP1	9.00	100, 300	CU	30	17.8/13.7	17	37.6
JAP1	11.00	100, 200	CU	32	14.4/10.9	10	37.1
JAP1	14.50	100, 300	CU	34	17.0/12.7	20	38.0

[1] γ_d Dry density.

The studied soils have friction angle ($\varnothing'$) values that are slightly lower and cohesion values (c′) that are much lower than those of the volcanic soils analyzed by O'Rourke and Crespo [2]. This is justified to a certain degree, given that they are similar in structure, although from a different formation. The soils examined by O'Rourke and Crespo [2] were in an area between the sectors of Tumbaco and the Chillos Valley, to the east of Quito, while those in the present study are from the north-central region of the city.

Figure 19a shows the variation profile of the peak friction angle ($\varnothing'_{peak}$) with depth for boreholes JAP1 and AMA1 according to the values given in Table 1. The tendency of the friction angle value to increase with depth can be clearly seen. It can also be seen that the Standard Penetration Test values (N_{SPT}) were correlated with the friction angle ($\varnothing'$), after which the linear regression analysis technique was adopted to obtain this relationship. Finally, the relationship with the best fit achieved in this process is shown in Figure 19b and Equation (8).

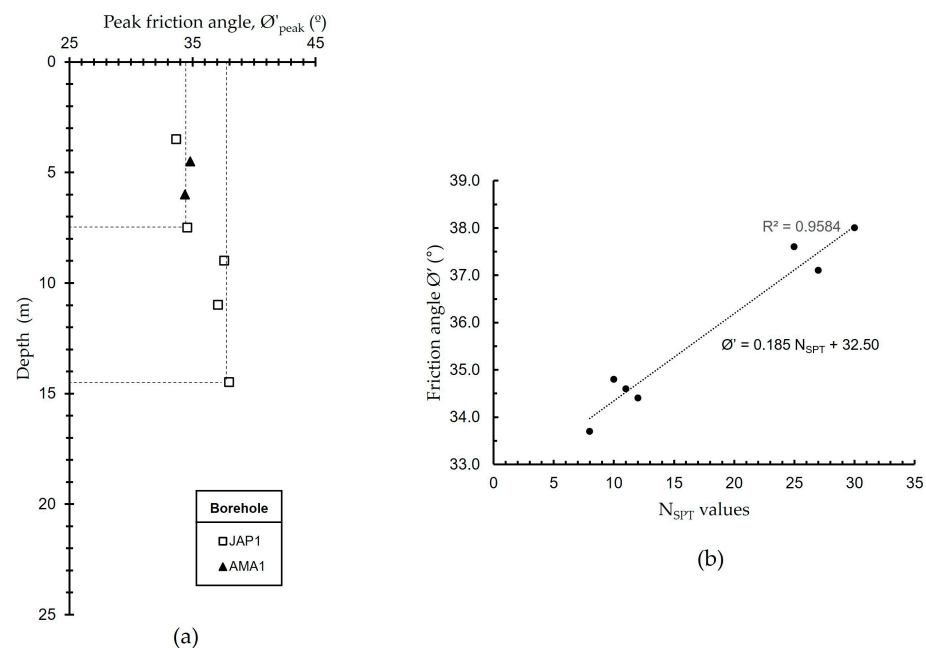$$\varnothing' = 0.185 \, N_{SPT} + 32.50 \tag{8}$$

Figure 19. (**a**) Peak friction angles estimated in triaxial testing for boreholes JAP1 and AMA1; (**b**) correlation between N_{SPT} values and friction angle ($\varnothing'$).

3.4.2. Drained Shear Strength Properties

The drained strength of the soil is represented by the parameters of effective cohesion (c′) and the effective friction angle (Ø′) and is used for long-term analysis. As part of this research, consolidated-drained (CD) triaxial tests with volume change measurements were also performed on 38 mm diameter and 76 mm height specimens per ASTM D7181 specification [73] recommendations. In this type of triaxial test, during the compression rupture phase of the specimen, the external pressure of the cell is kept constant, and the free drainage of the sample is left at a constant strain rate.

Each triaxial test comprised three successive stages: (1) saturation, (2) consolidation, and (3) rupture under drained conditions. The saturation stage of each specimen was carried out for 24 h, and at the end of the stage, it was verified that Skempton's B parameter was greater than 0.96. The consolidation stage was carried out under isotropic conditions, with pore water drainage at the top of the specimen. Finally, the rupture stage was performed under drained conditions and with a vertical displacement velocity of 0.01 mm/min.

Figure 20 shows the axial unitary stress–strain curves, q-ε_s, with the variation in the volume change for each of the samples from boreholes JAP1 and AMA1.
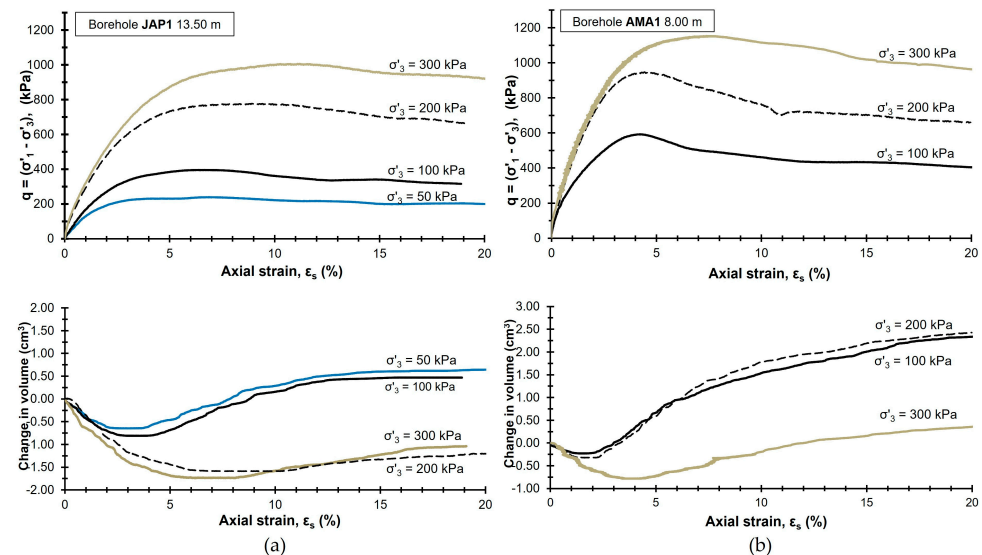

Figure 20. Stress–strain–volume-change curves for JAP1 and AMA1 samples.

A summary of the strength parameters obtained from consolidated-drained triaxial compression (CD) tests of JAP1 and AMA1 specimens is presented in Table 2. The tests performed show a peak friction angle of $\varnothing'_{peak} \approx 37°$ and an effective cohesion (c′) between 20 kPa and 69 kPa.

Table 2. Drained shear strength parameters for borehole samples JAP1 and AMA1.

Borehole	Test Depth (m)	Cell Pressure (kPa)	Triaxial Test	w_{nat} (%)	γ/γ_d [1] (kN/m³)	c′ (kPa)	Ø′ (°)
AMA1	8.00	100, 200, 300	CD	16	20.3/17.5	69	36.1
JAP1	13.50	50, 100, 200, 300	CD	31	19.1/14.6	20	36.9

[1] γ_d Dry density.

3.5. Deformation Parameters

The basic deformation parameters can be derived from the stress–strain curves, q-ε_s. In this way, the drained, E_i, and undrained, E_{ui}, moduli of elasticity and the secant modulus at 50% of the failure stress, E_{50}, can be obtained. Duncan and Chang [74] introduced a failure stress ratio of $R_f = (\sigma_1 - \sigma_3)_f/(\sigma_1 - \sigma_3)_{ult}$, because $(\sigma_1 - \sigma_3)_f$ is generally less than

$(\sigma_1 - \sigma_3)_{\text{ult}}$, where $(\sigma_1 - \sigma_3)_f$ is the deviatoric stress at failure, and $(\sigma_1 - \sigma_3)_{\text{ult}}$ is the last asymptotic value of the deviatoric stress in the triaxial test.

The relationship between these different parameters can be seen in Plaxis [46]. By way of example, the parameter E_{50} is the confining stress-dependent stiffness modulus for primary loading and is obtained by Equation (9).

$$E_{50} = E_{50}^{\text{ref}} \left(\frac{c'\cos\varnothing' - \sigma'_3\sin\varnothing'}{c'\cos\varnothing' + p^{\text{ref}}\sin\varnothing'} \right)^{m} \tag{9}$$

where E_{50}^{ref} is a reference secant stiffness modulus corresponding to the reference confining pressure p^{ref}, and m is the stress dependence relationship in the stiffness behavior, while E_i^{ref} is the drained stiffness modulus at the reference pressure, and E_{ui}^{ref} is the undrained stiffness modulus at the reference pressure.

The deformation parameters obtained from the stress paths for a reference pressure p^{ref} of 100 kPa for the consolidated-undrained triaxial compression tests (CU) are given in Table 3, while Table 4 shows the deformation parameters for the consolidated-drained triaxial compression tests (CD).

Table 3. Deformation parameters of controlled stress paths of triaxial CU-type tests of JAP1 and AMA1 borehole samples.

			Tangent Modulus		Secant Modulus			
Test		p^{ref}	E_{ui}^{ref}	m	$E_{50(u)}^{\text{ref}}$ [1]	m	$E_{ui}^{\text{ref}}/E_{50(u)}^{\text{ref}}$	R_f
Borehole	**Depth (m)**	**(kPa)**	**(kPa)**	**(-)**	**(kPa)**	**(-)**	**(-)**	**(-)**
JAP1	3.50	100	20,000	1.20	7353	1.54	2.72	0.98
AMA1	4.50	100	41,667	0.81	11,364	1.27	3.67	0.92
AMA1	6.00	100	55,556	1.05	45,455	1.11	1.22	0.99
JAP1	7.50	100	32,258	0.73	14,085	1.11	2.29	0.97
JAP1	9.00	100	51,020	0.90	12,500	0.80	4.08	0.75
JAP1	11.00	100	52,632	1.21	21,277	0.93	2.47	0.92
JAP1	14.50	100	41,379	0.73	18,462	0.96	2.24	0.91

[1] $E_{50(u)}^{\text{ref}}$ Secant stiffness modulus at reference pressure in an undrained triaxial test.

Table 4. Deformation parameters of CD-type triaxial tests of JAP1 and AMA1 borehole samples.

			Tangent Modulus		Secant Modulus			
Test		p^{ref}	E_i^{ref}	m	E_{50}^{ref} [1]	m	$E_i^{\text{ref}}/E_{50}^{\text{ref}}$	R_f
Borehole	**Depth (m)**	**(kPa)**	**(kPa)**	**(-)**	**(kPa)**	**(-)**	**(-)**	**(-)**
JAP1	13.50	100	25,000	0.60	16,815	0.59	1.49	0.99
AMA1	8.00	100	85,714	0.60	32,370	0.60	2.65	0.99

[1] E_{50}^{ref} Secant stiffness modulus at reference pressure in a drained triaxial test.

3.6. Discussion of the Geotechnical Characterization Study

This study's soil classification is consistent with the volcanic soil classifications of other researchers, as is the case with Hürlimann et al. [14], who worked with soils in Tenerife, Canary Islands (Spain), and mainly identified them as silty sands (SM); Crosta et al. [10], who investigated the volcanic soils of the Santa Tecla (El Salvador) zone and recognized the presence of low to high-plasticity silts (ML and MH), medium-plasticity clays (CL), and silty sands (SM); and Brandes and Nakayama [13], who studied the volcanic soils in the islands of Oahu and Hawaii (USA), which were identified as medium-to-high plasticity silts (ML and MH) and high-plasticity clays (CH) and silty sands (SM).

The presence of mainly plagioclases and pyroclastic materials of andesitic composition was identified through mineralogy and microstructure analyses; silica, a principal cementing agent, was also found to be present.

With regard to the parameters obtained from the oedometric tests, the C_c soil values in this study (0.06–0.36) are similar to those determined by Hürlimann et al. [14] for the

volcanic soils of Tenerife (Spain), where the value for this index was 0.287. Conversely, the C_c value range of this survey is similar to the C_c value of 0.22 obtained for volcanic soils identified as medium-plasticity red silt (ML) from Kapolei, Hawaii (USA), and much less than the C_c value of 0.49 for the high-plasticity brown clay (CH) in this same zone obtained by Brandes and Nakayama [13].

In this study, in general, the $\emptyset'_{peak}$ obtained shows a minimum value of 33.7° at a depth of 3.5 m, gradually increasing with depth to 38.0° at 14.5 m. Two separate groups are clearly identifiable. Between 3.5 m and 7.5 m, the measured $\emptyset'_{peak}$ values range from 33.7° to 34.8°, with an average value of 35°. At depths between 9 m and 14.5 m, the measured $\emptyset'_{peak}$ values range from 37.1° to 38.0°, with an average value of 38°. The friction angle values are slightly less than those of the volcanic soil values found by O'Rourke and Crespo [2] in the eastern zone of the city of Quito (Ecuador), which ranged between 39° and 40°, while the values obtained in this study are within the range for the Tenerife, Canary Islands (Spain), volcanic soils analyzed by Hürlimann et al. [14], which were between 30° and 40°. In the same manner, the friction angle values for this study are very similar to those of the volcanic soils studied in San Salvador (El Salvador) by Bommer et al. [9], which varied between 35° and 40°. Conversely, the $\emptyset'_{peak}$ friction angle values for this study are similar to the value of 32.7° determined for the red medium-plasticity silts in Kapolei, Hawaii (USA), and greater than the value of 23.4° obtained from the brown high-plasticity clay in this same region studied by Brandes and Nakayama [13].

The cohesion values obtained in the present study (5 to 26 kPa) are very similar to those of the volcanic soils in San Salvador (El Salvador) investigated by Bommer et al. [9], which oscillated between 25 kPa and 30 kPa. Furthermore, the values obtained in this study are seen to be within the range of the volcanic soils from Isparta (Turkey) studied by Avşar et al. [16], which ranged between 0 and 52 kPa, as can be seen in Table 5. The cohesion values of the volcanic soils in Java (Indonesia) derived from the weathering of volcanic deposits and volcanic ash were determined by Wesley [75] to be between 13 kPa to 14 kPa, which fits within the range of the values obtained in this study.

Table 5. Comparison of the geotechnical properties with those of volcanic soils studied by other research groups. Modified Table from Avşar et al. [16].

Researcher(s)	Soil Description	Location/ Country	Specific Gravity G_s	Bulk Density (Mg/m³)	Void Ratio e	Porosity n (%)	Triaxial Test (CU/CD) c' (kPa)	Ø' (°)	Peak Shear Strength. Tx (UU) c (kPa)	Ø (°)	Direct Shear Test c (kPa)	Ø (°)
O'Rourke and Crespo [2]	Volcaniclastic deposit	Eastern Quito/ Ecuador	2.58–2.59	1.31–1.69	0.76–1.30	43–56	111–201	39–40	-	-	-	-
Hürlimann et al. [14]	Volcanic residual soil	Canary Islands/ Spain	2.70 [1]	1.53	1.20–1.60	54–60	-	-	-	-	0	30–45
Bommer et al. [9]	Volcanic soil, pyroclastic and epiclastic deposit	Tierra Blanca/ El Salvador	2.25–2.50	1.33–1.53	0.80–1.14	51	-	-	-	-	25–30	35–40
Crosta et al. [10]	Weakly to moderately cemented volcanic soil (pyroclastic)	Santa Tecla/ El Salvador	1.90–2.70	1.52	-	-	-	-	8–950	3.2–39.6	7–13	20.5–29.2
Avşar et al. [16]	Weakly bonded volcanic deposit	Isparta/ Turkey	2.35–2.65	1.43–1.70	0.49–0.85 [2]	33–46	-	-	-	-	0–52	41–59
This study	Volcanic soil	Northern Quito/ Ecuador	2.35–2.70	1.44–2.03	0.49–1.92	33–66	5–26	34–38	-	-	-	-

[1] Value taken from Avşar et al.'s [16] study. [2] Values calculated according to porosity values.

4. Analysis of a Soil Nailing Structure Built in the Area of Study

4.1. Structure Characteristics

The studied structure is named the Zaigen Building and is located in the north-central area of the city of Quito, precisely in the JAP1 drilling area. It has five underground car park levels and a total excavation of 15.50 m, achieved by means of five partial excavations (h = 3.10 m) that represent the height of a basement level, as shown in Figure 21. In this numerical model, using the finite element method with Plaxis 2D [44–46], a small surface overload of 1 kN/m has been included in the roadway to consider the light and sporadic vehicular traffic during the construction process. Figure 21a presents the initial numerical model for the Soil Nailing structure, including dimensions, structural elements, and other parameters that characterize this structure. Figure 21b shows the numerical model in the fifth phase of excavation, which is when underground level 5 had already been built and a total excavation of 15.50 m had been completed. Additionally, the construction of each basement level includes four basic construction phases: (1) the initial excavation of the entire basement level (h = 3.10 m), leaving a small soil buttress, (2) the construction of the Soil Nail, (3) the vertical shaping of the slope, and (4) the construction of the concrete facing.
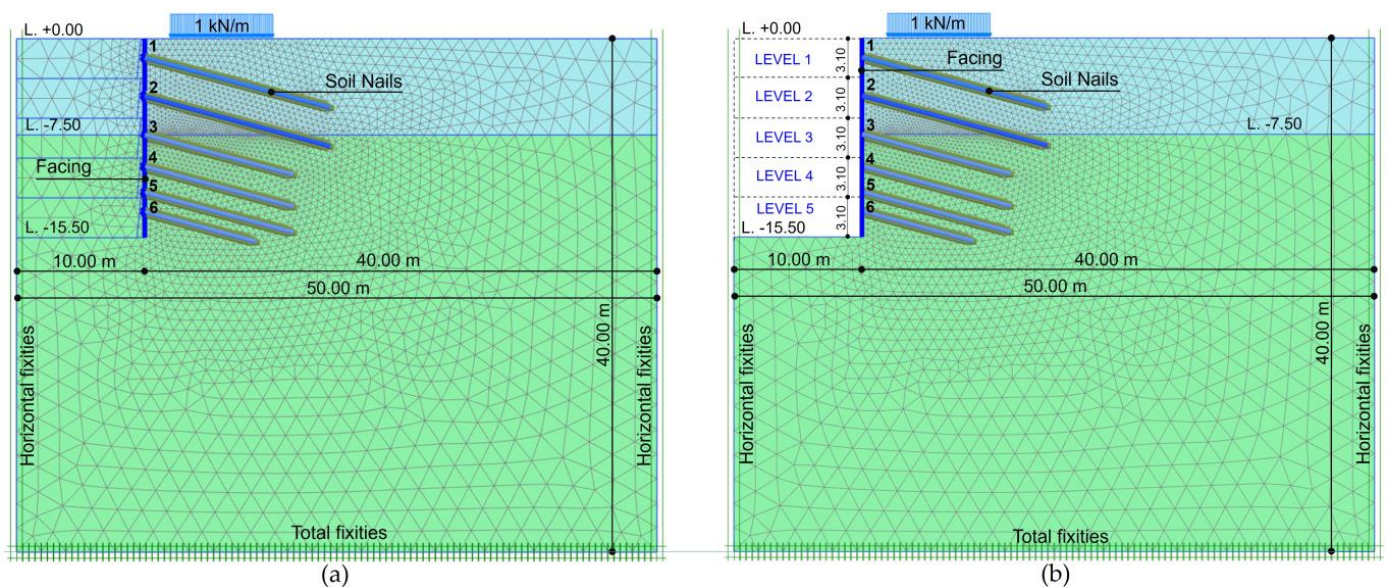

Figure 21. Soil Nailing structure model with Plaxis 2D [44,45]: (**a**) initial model; (**b**) final model.

To generate a finite element mesh with an appropriate density, 15-node elements were used. A "very fine" element mesh was generated to obtain accurate numerical results. The initial stresses for the model taking the loading history of the soils into account were generated using the K_0 procedure. Furthermore, standard interfaces in the Soil Nails have been included in the model to consider and simulate the existing friction in the soil–anchor interaction [45]. The value considered for the strength of the interfaces was R_{inter} = 0.67.

4.2. Geotechnical Parameters

The geotechnical characterization study determined that the project area's subsoil consists of volcanic soils containing mainly silts and clays with low-to-high plasticity and silty sands. Two main soil strata were identified (0–7.5 m and 7.5–15.5 m), for which the respective geotechnical parameters were determined. Soil strength parameters were determined through CU and CD triaxial testing, while the stiffness parameters were determined exclusively through CD triaxial testing. Table 6 shows the parameters determined for the application of the Mohr–Coulomb (MC) soil constitutive model. Table 7 shows the parameters for the Hardening Soil (HS) constitutive model.

Table 6. Geotechnical parameters for the Mohr–Coulomb (MC) constitutive model.

Parameter	Depth	
	0–7.50 m	**7.50–15.50 m**
Effective cohesion, c' (kN/m^2)	18	17
Effective friction angle, $\emptyset'$ (°)	34	36
Angle of dilatancy, ψ (°)	4	6
Soil unit weight, γ (kN/m^3)	17.0	17.5
Young's modulus, E' (kN/m^2)	20,000	25,000
Poisson's ratio, ν' (-)	0.3	0.3
Overconsolidation ratio, OCR (-)	1.6	1.3
Coefficient of earth pressure at rest of the overconsolidated soil, K_0 (-)	0.555	0.461

Table 7. Geotechnical parameters for the Hardening Soil (HS) constitutive model.

Parameter	Depth	
	0–7.50 m	**7.50–15.50 m**
Effective cohesion, c' (kN/m^2)	18	17
Effective friction angle, $\emptyset'$ (°)	34	36
Angle of dilatancy, ψ (°)	4	6
Soil unit weight, γ (kN/m^3)	17.0	17.5
Secant stiffness in drained triaxial test, E_{50}^{ref} (kN/m^2)	11,268	16,815
Tangent stiffness for primary oedometer loading, E_{oed}^{ref} (kN/m^2)	9140	8683
Unloading/reloading stiffness, E_{ur}^{ref} (kN/m^2)	33,804	90,314
Reference stress for stiffness, p^{ref} (kN/m^2)	100	100
Power for stress-level dependency of stiffness, m (-)	0.60	0.60
Poisson's ratio for unloading/reloading, ν_{ur} (-)	0.20	0.20
Coefficient of lateral stress in normal consolidation, K_0^{NC} (-)	0.441	0.412
Overconsolidation ratio, OCR (-)	1.6	1.3
Coefficient of earth pressure at rest of the overconsolidated soil, K_0 (-)	0.555	0.461

The application of the Hardening Soil with Small-Strain Stiffness (HSsmall) soil constitutive model requires the same parameters as the Hardening Soil model and also the additional parameters presented in Table 8 [46].

Table 8. Additional geotechnical parameters for HSsmall constitutive model.

Parameter	Depth	
	0–7.50 m	**7.50–15.50 m**
Shear modulus at very small strains, G_0^{ref} (kN/m^2)	45,596	77,132
Shear strain at which G = 0.7 G_0, γ 0.7 (-)	5.28×10^{-4}	4.85×10^{-4}

4.3. Characteristics of the Facing and Soil Nails

Tables 9 and 10 show the parameters of axial stiffness EA, flexural rigidity EI, and unit weight w for the facing and the Soil Nails. The parameters for the facing were calculated for

a unit length of 1 m and for a concrete unit weight of 24 kN/m^3. In order to obtain the Soil Nail parameters, an equivalent modulus of elasticity was initially determined considering the cross-section composed of steel and grout, and then the stiffness values were obtained for each row as a function of the horizontal spacing of the Soil Nails, as shown in Table 10.

Table 9. Geometric characteristics and other parameters of the Soil Nailing structure.

Parameter	Value
Soil Nails and Shotcrete model	Elastic
Facing	
Vertical wall height (m)	15.50
Wall or facing thickness (m)	0.25
Modulus of elasticity of Concrete (MPa)	22,800
Axial stiffness, EA (kN/m)	5,700,000
Flexural rigidity, EI (kN.m^2/m)	29,685
Unit weight, w (kN/m/m)	6.00
Soil Nails	
Modulus of elasticity of Soil Nail steel (MPa)	200,000
Modulus of elasticity of Soil Nail grout (MPa)	21,320
Borehole diameter (m)	0.15
Soil Nail rebar diameter (mm)	25
Soil Nail inclination in relation to horizontal plane (°)	15

Table 10. Axial stiffness EA, flexural rigidity EI, and unit weight w of Soil Nails.

Basement Level	Soil Nail Row	Soil Nail Length (m)	Horizontal Separation (m)	Axial Stiffness EA (kN/m)	Flexural Rigidity EI (kN.m^2/m)	Unit Weight w (kN/m/m)
1	1	15.0	2.00	232,203	327	0.208
2	2	15.0	1.70	273,180	384	0.245
3	3	12.0	1.60	290,254	408	0.260
4	4	12.0	1.60	290,254	408	0.260
	5	12.0	1.60	290,254	408	0.260
5	6	9.0	1.60	290,254	408	0.260

4.4. Structure Analysis with Plaxis 2D: Discussion of Results

Figure 22 presents the analysis of the structure for the construction of basement 5.

The construction of basement level 5 produced a total height of 15.5 m on the facing. It is therefore the construction phase associated with the greatest degree of displacements and stresses. It is clear from the analysis with the three constitutive soil models that excavation with the Mohr–Coulomb (MC) model presents very high soil uplift values at the bottom of the excavation, which is a situation that is not realistic, in contrast to the analysis with the HSsmall model, which determined low soil uplift values at the bottom of the excavation and is closer to reality. On the other hand, the Hardening Soil (HS) model presents uplift values in an intermediate range that falls between the analyses with MC and HSsmall, as can be seen in Figure 22. Figures 23 and 24 show the distribution of axial tension forces in the Soil Nails and the displacements induced by the construction of basement level 5, respectively.
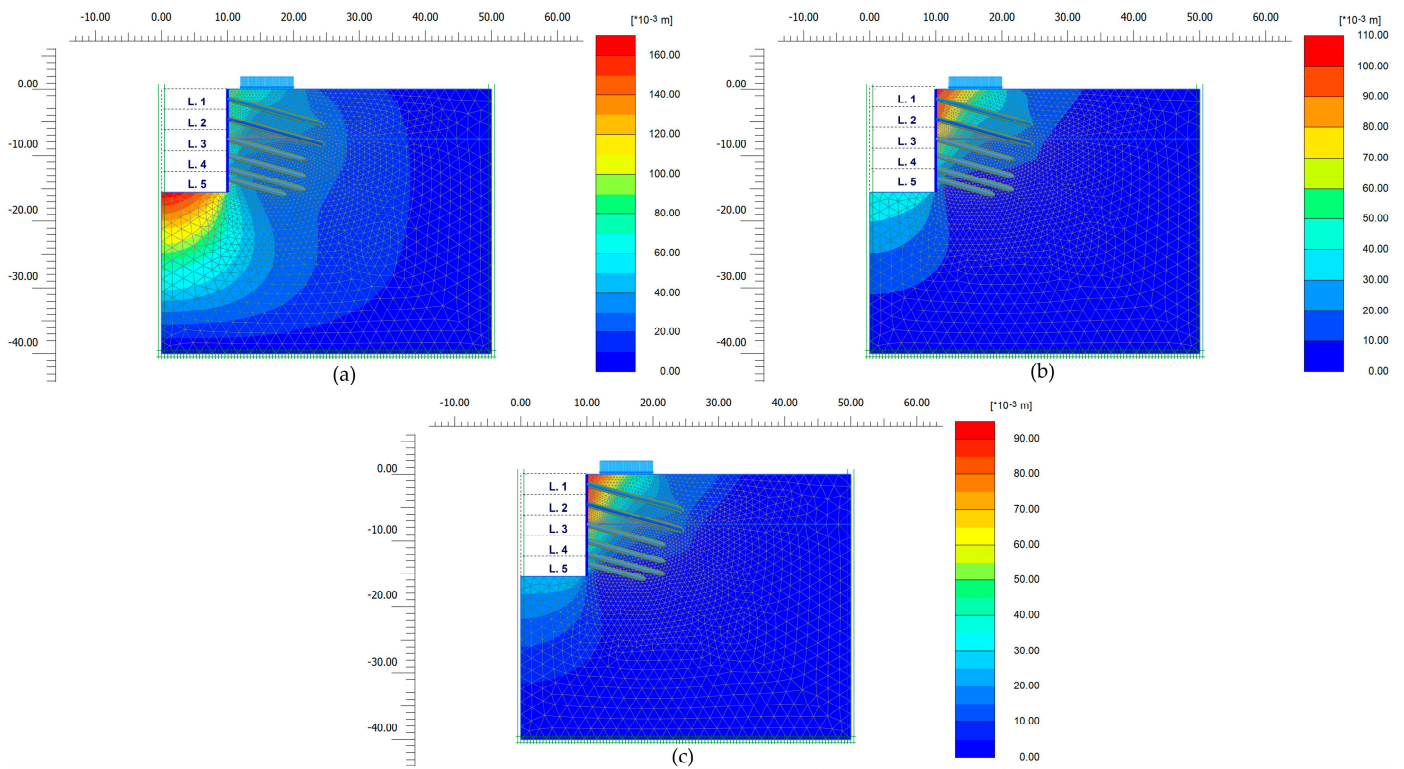
Figure 22. Total displacements induced by construction of basement level 5 with soil model: (**a**) Mohr–Coulomb; (**b**) Hardening Soil; (**c**) HSsmall.
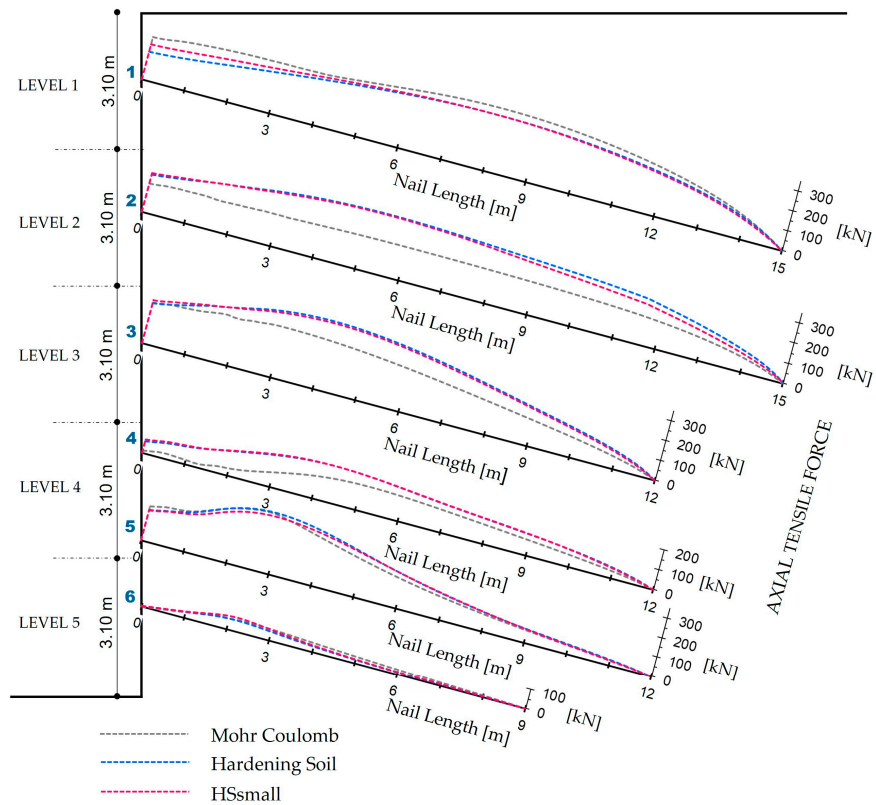

Figure 23. Distribution of axial tensile forces in Soil Nails induced by construction of basement level 5.
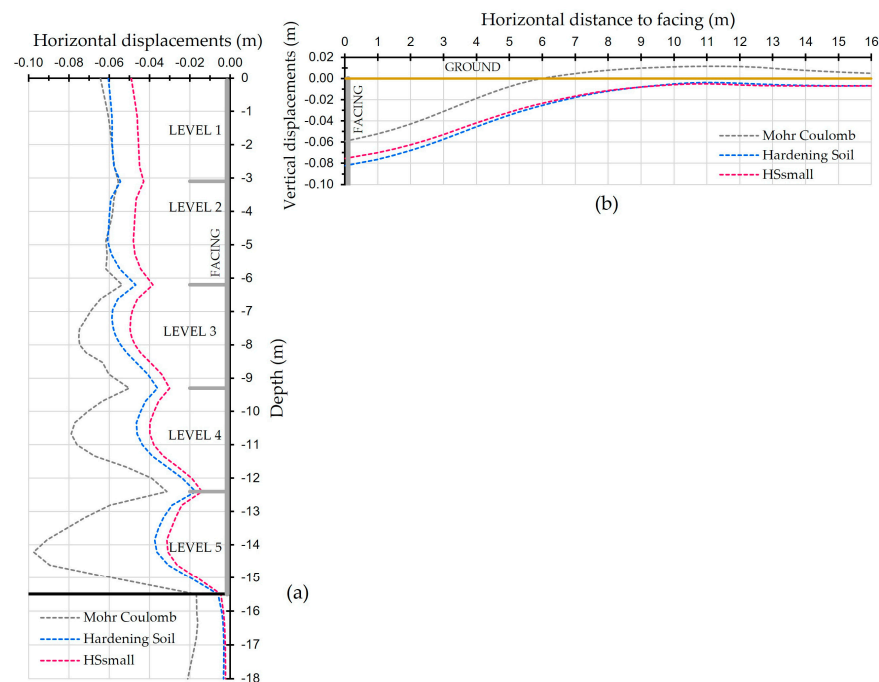
Figure 24. Displacements induced by the construction of basement 5: (**a**) horizontal facing displacements; (**b**) vertical ground displacements.

The tensile force magnitudes determined for the Soil Nails with the Mohr–Coulomb constitutive model are generally lower than the stresses determined with the Hardening Soil and HSsmall models. However, the forces obtained with Hardening Soil and HSsmall have some similarities between them for most of the process, with the Hardening Soil stresses being slightly higher in most of the construction phases, as can be seen in Figure 23. Accurately estimating the maximum tensile strength that a Soil Nail can sustain throughout its service life is a crucial aspect of the final design of a Soil Nailing structure. This step considers the ultimate limit states of the pullout and tensile strength of the Soil Nails [76]. Achieving precision in estimating the pullout capacity of a Soil Nail is essential to ensure a cost-effective, efficient, and safe design [77,78]. Therefore, it underscores the importance of adopting an appropriate soil constitutive model for the geotechnical analysis of a Soil Nailing structure.

For most of the construction stages, the horizontal facing displacements determined with the Mohr–Coulomb model are the lowest, unlike the horizontal displacements obtained with Hardening Soil, which are greater than the rest, while the values with HSsmall remain in an intermediary position.

Vertical displacements or settlements of the soil behind the facing, as determined with the Mohr–Coulomb model resulted mainly in states of soil rising or uplift rather than settlements, because this constitutive soil model uses a single modulus of soil elasticity for loading and unloading. On the other hand, the analyses of vertical displacements with the Hardening Soil and HSsmall soil constitutive models both determined similar values of settlements induced by the construction of the basement levels, with the Hardening Soil settlements being slightly higher. The settlements obtained with these two constitutive soil models are expected to be more realistic, since they additionally include an unloading/reloading stiffness modulus, E_{ur}, which allows for the representation of the behavior of the soil under loading and unloading conditions.

Figure 25 and Table 11 present the Factor of safety (FoS) variation during the construction progress of each basement level. A comparison of the three different constitutive soil model analyses was made through the finite element method with Plaxis 2D [44,45] and different limit equilibrium methods with Slide2 [79].
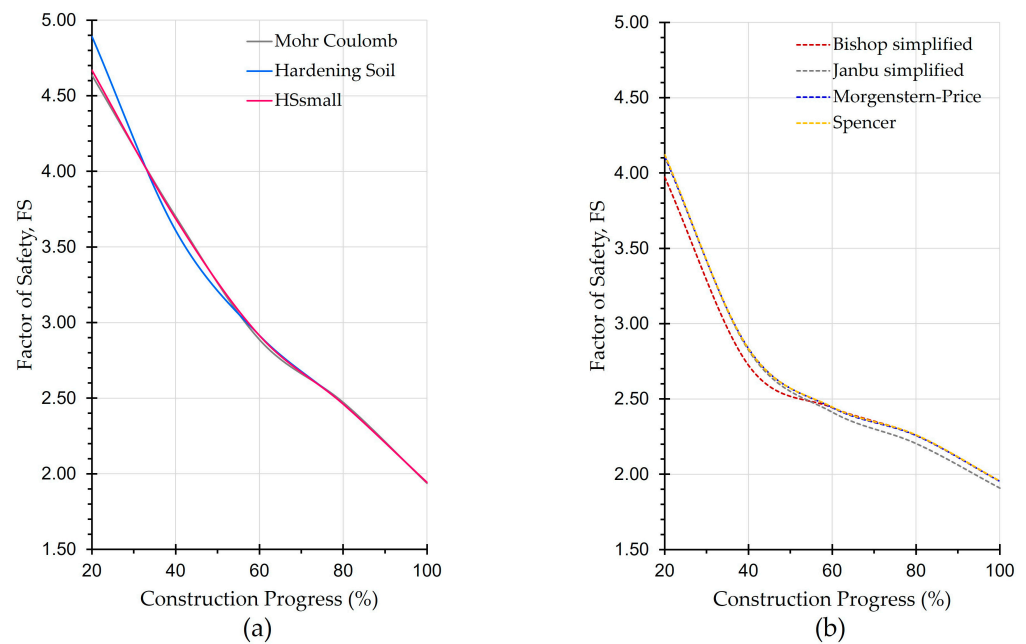
Figure 25. Factor of safety (FoS) variations during the construction progress of basement levels: (**a**) finite element method; (**b**) limit equilibrium methods.

Table 11. Factor of safety (FoS) variations with basement-level construction progress.

| Basement Level Construction Progress (%) | Finite Element Method | | | Limit Equilibrium Methods | | | |
	Mohr–Coulomb	Plaxis 2D Hardening Soil	HSsmall	Bishop Simplified	Slide2 Janbu Simplified	Morgenstern Price	Spencer
1 (20%)	4.64	4.89	4.67	3.97	4.12	4.11	4.12
2 (40%)	3.70	3.61	3.69	2.72	2.82	2.84	2.83
3 (60%)	2.89	2.92	2.91	2.44	2.41	2.44	2.45
4 (80%)	2.47	2.46	2.46	2.26	2.20	2.26	2.26
5 (100%)	1–94	1.94	1.94	1.95	1.91	1.95	1.95

Both methodologies provided a satisfactory analysis of the nailed facing stability. However, the FoS determined with finite elements and limit equilibrium presented disparate values at the beginning of the basement-level construction; however, these values converged as the construction progressed, eventually arriving at similar values at the end of the construction of the fifth basement level, with similar potential failure surfaces.

5. Conclusions

Geotechnical characterization studies are fundamental in the evaluation and analysis of landslides, particularly in urban environments, where significant stabilization works are undertaken as ground reinforcement. Precise knowledge of the geotechnical properties of the materials within an earth structure is useful to comprehend its failure mechanism and determine the appropriate geological model, allowing for the selection of the most suitable soil constitutive model to accurately represent the actual conditions.

In this study, we took an application-based approach to Soil Nailing structures, which are frequently used in reinforcing excavations for the construction of underground basements in buildings in the city of Quito. This method has been technically used worldwide, but in many cases in the Ecuadorian capital, it is still applied in a traditional and artisanal manner. Globally, the technique has been used in different soil types, but it is not easy to find specific studies for this type of structure in volcanic soils.

The Soil Nailing structure presented herein was analyzed with advanced soil constitutive models using the finite element method. The main advantage of an analysis using the

finite element method is a detailed analysis of soil deformations, unlike limit equilibrium methods, which do not permit this type of analysis.

The HSsmall and Hardening Soil constitutive soil models better reproduced the behavior of Soil Nailing structures; however, their application requires specialized testing, such as CU and CD triaxial tests, which are necessary to determine the shear strength parameters, with the additional consideration that CD triaxial testing is mandatory to determine stiffness parameters. Furthermore, oedometric testing is necessary for the application of these soil models to obtain the tangent stiffness moduli. This study included, among others, all of the previously mentioned tests.

Finally, the area of study is generally characterized by volcanic soils with high void ratios and porosity resulting from the natural presence of gas bubbles in their microstructures. In such soils, initial shear strength parameters are identified that greatly favor the stability of cut slopes generated by human activity. However, earth structures consisting of such materials that are not equipped with an adequate protection or lining system to safeguard against external agents, particularly rain, could experience a sudden and accelerated reduction in their shear strength characteristics if microscopic gas bubbles are filled with water, causing the main structure to collapse.

In summary, comprehensive geotechnical characterization studies will allow for determining parameters to reproduce the geological conditions of a specific area through a coherent theoretical model, aimed at analyzing its stability and successfully preventing landslides. Moreover, an understanding of these soils in terms of their behavior and potential failure mechanism means that recommendations can be made concerning the best type of reinforcement and stabilization systems for earth structures developed in a particular area, with an emphasis on urban environments.

References

1. Capa, V.E. Estudio Experimental y Numérico del Comportamiento de Excavaciones Ejecutadas Mediante la Técnica de Suelo Claveteado (Soil Nailing) en Suelos de la Ciudad de Quito (Ecuador). Ph.D. Thesis, Universitat Politècnica de València, Valencia, Spain, 2021. [CrossRef]
2. O'Rourke, T.D.; Crespo, E. Geotechnical Properties of Cemented Volcanic Soils. *J. Geotech. Eng.* **1988**, *114*, 1126–1147. [CrossRef]
3. Belloni, L.; Morris, D. Earthquake-induced shallow slides in volcanic debris soils. *Géotechnique* **1991**, *41*, 539–551. [CrossRef]
4. Vezzoli, L.; Apuani, T.; Corazzato, C.; Uttini, A. Geological and geotechnical characterization of the debris avalanche and pyroclastic deposits of Cotopaxi Volcano (Ecuador). A contribute to instability-related hazard studies. *J. Volcanol. Geotherm. Res.* **2017**, *332*, 51–70. [CrossRef]

5.   Bablon, M.; Quidelleur, X.; Samaniego, P.; Le Pennec, J.L.; Santamaría, S.; Liorzou, C.; Hidalgo, S.; Eschbach, B. Volcanic history reconstruction in northern Ecuador: Insights for eruptive and erosion rates on the whole Ecuadorian arc. *Bull. Volcanol.* **2020**, *82*, 11. [CrossRef]

6.   Santamaria, S.; Quidelleur, X.; Hidalgo, S.; Samaniego, P.; Le Pennec, J.; Liorzou, C.; Lahitte, P.; Córdova, M.; Espín, P. Geochronological evolution of the potentially active Iliniza Volcano (Ecuador) based on new K-Ar ages. *J. Volcanol. Geotherm. Res.* **2022**, *424*, 107489. [CrossRef]

7.   Andrade, S.D.; Vásconez Müller, A.; Vasconez, F.J.; Beate, B.; Aguilar, J.; Santamaría, S. Pululahua dome complex, Ecuador: Eruptive history, total magma output and potential hazards. *J. S. Am. Earth Sci.* **2021**, *106*, 103046. [CrossRef]

8.   Nauret, F.; Samaniego, P.; Ancellin, M.; Tournigand, P.; Le Pennec, J.; Vlastelic, I.; Gannoun, A.; Hidalgo, S.; Schiano, P. The genetic relationship between andesites and dacites at Tungurahua volcano, Ecuador. *J. Volcanol. Geotherm. Res.* **2018**, *349*, 283–297. [CrossRef]

9.   Bommer, J.J.; Rolo, R.; Mitroulia, A.; Berdousis, P. Geotechnical properties and seismic slope stability of volcanic soils. In Proceedings of the 12th European Conference on Earthquake Engineering (Paper Ref. 695), London, UK, 9–13 September 2002.

10.   Crosta, G.B.; Imposimato, S.; Roddeman, D.; Chiesa, S.; Moia, F. Small fast-moving flow-like landslides in volcanic deposits: The 2001 Las Colinas Landslide (El Salvador). *Eng. Geol.* **2005**, *79*, 185–214. [CrossRef]

11.   González de Vallejo, L.I.; Hijazo, T.; Ferrer, M. Engineering Geological Properties of the Volcanic Rocks and Soils of the Canary Islands. *Soils Rocks* **2008**, *31*, 3–13. [CrossRef]

12.   del Potro, R.; Hürlimann, M. Geotechnical classification and characterisation of materials for stability analyses of large volcanic slopes. *Eng. Geol.* **2008**, *98*, 1–17. [CrossRef]

13.   Brandes, H.G.; Nakayama, D.D. Creep, strength and other characteristics of Hawaiian volcanic soils. *Géotechnique* **2010**, *60*, 235–245. [CrossRef]

14.   Hürlimann, M.; Ledesma, A.; Martí, J. Characterisation of a volcanic residual soil and its implications for large landslide phenomena: Application to Tenerife, Canary Islands. *Eng. Geol.* **2001**, *59*, 115–132. [CrossRef]

15.   Moon, V.; Bradshaw, J.; Smith, R.; de Lange, W. Geotechnical characterisation of stratocone crater wall sequences, White Island Volcano, New Zealand. *Eng. Geol.* **2005**, *81*, 146–178. [CrossRef]

16.   Avşar, E.; Ulusay, R.; Mutlutürk, M. An experimental investigation of the mechanical behavior and microstructural features of a volcanic soil (Isparta, Turkey) and stability of cut slopes in this soil. *Eng. Geol.* **2015**, *189*, 68–83. [CrossRef]

17.   Okewale, I.A.; Coop, M.R. A study of the effects of weathering on soils derived from decomposed volcanic rocks. *Eng. Geol.* **2017**, *222*, 53–71. [CrossRef]

18.   Yamanouchi, T.; Murata, H. Brittle failure of a volcanic ash soil "Shirasu". In Proceedings of the 8th International Conference on Soil Mechanics and Foundation Engineering, Moscow, Russia, 1973; Volume 1, pp. 495–500. Available online: https://www.issmge.org/publications/publication/brittle-failure-of-a-volcanic-ash-soil-shirasu (accessed on 14 May 2023).

19.   Thakur, M.; Kumar, N.; Dhiman, R.K.; Malik, J.N. Geological and geotechnical investigations of the Sataun landslide along the Active Sirmauri Tal Fault, Sataun, Northwestern Himalaya, India. *Landslides* **2023**, *20*, 1045–1063. [CrossRef]

20.   Cheung, R.W.M. Landslide risk management in Hong Kong. *Landslides* **2021**, *18*, 3457–3473. [CrossRef]

21.   Cook, M.E.; Brook, M.S.; Hamling, I.J.; Cave, M.; Tunnicliffe, J.F.; Holley, R.; Alama, D.J. Engineering geomorphological and InSAR investigation of an urban landslide, Gisborne, New Zealand. *Landslides* **2022**, *19*, 2423–2437. [CrossRef]

22.   Turner, A.K.; Schuster, R.L. *Landslides: Investigation and Mitigation*; National Academy Press: Washington, DC, USA, 1996.

23.   Erginal, A.E.; Türkes, M.; Ertek, T.A.; Baba, A.; Bayrakdar, C. Geomorphological investigation of the excavation-induced Dündar landslide, Bursa-Turkey. *Geogr. Ann.* **2008**, *90*, 109–123. [CrossRef]

24.   Ayalew, L.; Moeller, D.; Reik, G. Geotechnical Aspects and Stability of Road Cuts in the Blue Nile Basin, Ethiopia. *Geotech. Geol. Eng.* **2009**, *27*, 713–728. [CrossRef]

25.   Zhang, F.; Liu, G.; Chen, W.; Liang, S.; Chen, R.; Han, W. Human-induced landslide on a high cut slope: A case of repeated failures due to multi-excavation. *J. Rock Mech. Geotech. Eng.* **2012**, *4*, 367–374. [CrossRef]

26.   Burland, J.B.; Longworth, T.I.; Moore, J.F.A. A study of ground movement and progressive failure caused by a deep excavation in Oxford Clay. *Geotechnique* **1977**, *27*, 557–591. [CrossRef]

27.   Tsidzi, K.E.N. An engineering geological approach to road cutting slope design in Ghana. *Geotech. Geol. Eng.* **1997**, *15*, 31–45. [CrossRef]

28.   Bozzano, F.; Martino, S.; Priori, M. Natural and man-induced stress evolution of slopes: The Monte Mario hill in Rome. *Environ. Geol.* **2006**, *50*, 505–524. [CrossRef]

29.   Fuentes, R.; Pillai, A.; Ferreira, P. Lessons learnt from a deep excavation for future application of the observational method. *J. Rock Mech. Geotech. Eng.* **2018**, *10*, 468–485. [CrossRef]

30.   Lee, S.G.; Hencher, S.R. The repeated failure of a cut-slope despite continuous reassessment and remedial works. *Eng. Geol.* **2009**, *107*, 16–41. [CrossRef]

31.   Ehrlich, M.; Silva, R.C. Behavior of a 31 m high excavation supported by anchoring and nailing in residual soil of gneiss. *Eng. Geol.* **2015**, *191*, 48–60. [CrossRef]

32.   Liao, Y.; Derrega, S.M.; Hall, C.A. A case history study on causation of the landslide in Santa Clara, California, USA. *J. Rock Mech. Geotech. Eng.* **2015**, *7*, 185–192. [CrossRef]

33. Turner, J.P.; Jensen, W.G. Landslide Stabilization Using Soil Nail and Mechanically Stabilized Earth Walls: Case Study. *J. Geotech. Geoenviron. Eng.* **2005**, *131*, 141–150. [CrossRef]

34. Villalobos, S.A.; Oróstegui, P.L.; Villalobos, F.A. Re-assessing a soil nailing design in heavily weathered granite after a strong earthquake. *Bull Eng. Geol. Environ.* **2013**, *72*, 203–212. [CrossRef]

35. Zhu, F.; Miao, L.; Gu, H.; Cheng, Y. A case study on behaviors of composite soil nailed wall with bored piles in a deep excavation. *J. Cent. South Univ.* **2013**, *20*, 2017–2024. [CrossRef]

36. Menkiti, C.O.; Long, M.; Milligan, G.W.E.; Higgins, P. Soil Nailing in Dublin Boulder Clay. *Geotech. Geol. Eng.* **2014**, *32*, 1427–1438. [CrossRef]

37. Fan, C.C.; Luo, J.H. Numerical study on the optimum layout of soil-nailed slopes. *Comput. Geotech.* **2008**, *35*, 585–599. [CrossRef]

38. Singh, V.P.; Sivakumar Babu, G.L. 2D Numerical Simulations of Soil Nail Walls. *Geotech. Geol. Eng.* **2010**, *28*, 299–309. [CrossRef]

39. Wei, W.B.; Cheng, Y.M. Soil nailed slope by strength reduction and limit equilibrium methods. *Comput. Geotech.* **2010**, *37*, 602–618. [CrossRef]

40. Rabie, M. Performance of hybrid MSE/Soil Nail walls using numerical analysis and limit equilibrium approaches. *HBRC J.* **2016**, *12*, 63–70. [CrossRef]

41. Rawat, S.; Gupta, A.K. Analysis of a Nailed Soil Slope Using Limit Equilibrium and Finite Element Methods. *Int. J. Geosynth. Ground Eng.* **2016**, *2*, 34. [CrossRef]

42. Bayat, M.; Kosarieh, A.H.; Javanmard, M. Probabilistic Seismic Demand Analysis of Soil Nail Wall Structures Using Bayesian Linear Regression Approach. *Sustainability* **2021**, *13*, 5782. [CrossRef]

43. Capa, V.E.; Calderón, P.A.; Torrijo, F.J. Experimental and numerical study on the behavior of soil nailing excavations in volcanic soils. In Proceedings of the 20th International Conference on Soil Mechanics and Geotechnical Engineering, Sydney, Australia, 1–5 May 2022.

44. Plaxis. *Plaxis 2D, Geotechnical Engineering Software*; Plaxis: Delf, The Netherlands, 2020.

45. Plaxis. *Plaxis 2D Reference Manual*; Plaxis: Delf, The Netherlands, 2020.

46. Plaxis. *Plaxis Material Models*; Plaxis: Delf, The Netherlands, 2020.

47. Hall, M.L.; Samaniego, P.; Le Pennec, J.L.; Johnson, J.B. Ecuadorian Andes volcanism: A review of Late Pliocene to present activity. *J. Volcanol. Geotherm. Res.* **2008**, *176*, 1–6. [CrossRef]

48. Rodríguez-Peces, M.J.; Gordón-Pérez, D. Análisis automático de la susceptibilidad de las inestabilidades de laderas provocadas por terremotos en un sector de la Cordillera de Los Andes, Ecuador. *Rev. Soc. Geológica España* **2015**, *28*, 91–104.

49. Coltorti, M.; Ollier, C.D. Geomorphic and tectonic evolution of the Ecuadorian Andes. *Geomorphology* **2000**, *32*, 1–19. [CrossRef]

50. Spikings, R.; Simpson, G. Rock uplift and exhumation of continental margins by the collision, accretion, and subduction of buoyant and topographically prominent oceanic crust. *Tectonics* **2014**, *33*, 635–655. [CrossRef]

51. Robin, C.; Samaniego, P.; Le Pennec, J.L.; Fornari, M.; Mothes, P.; van der Plicht, J. New radiometric and petrological constraints on the evolution of the Pichincha volcanic complex (Ecuador). *Bull. Volcanol.* **2010**, *72*, 1109–1129. [CrossRef]

52. Robin, C.; Eissen, J.P.; Samaniego, P.; Martin, H.; Hall, M.; Cotten, J. Evolution of the late Pleistocene Mojanda-Fuya Fuya volcanic complex (Ecuador), by progressive adakitic involvement in mantle magma sources. *Bull. Volcanol.* **2009**, *71*, 233–258. [CrossRef]

53. Samaniego, P.; Barba, D.; Robin, C.; Fornari, M.; Bernard, B. Eruptive history of Chimborazo volcano (Ecuador): A large, ice-capped and hazardous compound volcano in the Northern Andes. *J. Volcanol. Geotherm. Res.* **2012**, *221–222*, 33–51. [CrossRef]

54. Winkler, W.; Villagómez, D.; Spikings, R.; Abegglen, P.; Tobler, S.; Egüez, A. The Chota basin and its significance for the inception and tectonic setting of the inter-Andean depression in Ecuador. *J. S. Am. Earth Sci.* **2005**, *19*, 5–19. [CrossRef]

55. Ego, F.; Sébrier, M.; Lavenu, A.; Yepes, H.; Egüez, A. Quaternary state of stress in the Northern Andes and the restraining bend model for the Ecuadorian Andes. *Tectonophysics* **1996**, *259*, 101–116. [CrossRef]

56. *Hoja Geológica Sangolquí 1980, Escala: 1:50000, Quito, Ecuador*; Instituto de Investigación Geológico y Energético (IIGE): Quito, Ecuador, 1980.

57. Martin-Gombojav, N.; Winkler, W. Recycling of Proterozoic crust in the Andean Amazon foreland of Ecuador: Implications for orogenic development of the Northern Andes. *Terra Nova* **2008**, *20*, 22–31. [CrossRef]

58. Ruiz, G.M.H.; Seward, D.; Winkler, W. Evolution of the Amazon Basin in Ecuador with special reference to hinterland tectonics: Data from zircon fission-track and heavy mineral analysis. *Dev. Sedimentol.* **2007**, *58*, 907–934. [CrossRef]

59. *Estudio Geológico-Geotécnico para la Línea 1 del Metro de la Ciudad de Quito, Ecuador*; Empresa Pública Metropolitana Metro de Quito (EPMMQ): Quito, Ecuador, 2016.

60. Mujtaba, H.; Farooq, K.; Sivakugan, N.; Das, B. Evaluation of Relative Density and Friction Angle Base on SPT-N Values. *KSCE J. Civ. Eng.* **2017**, *22*, 572–581. [CrossRef]

61. *ASTM D1586-2011*; Standard Test Method for Standard Penetration Test (SPT) and Split-Barrel Sampling of Soils. ASTM International: West Conshohocken, PA, USA, 2011.

62. Laad, C.C.; DeGroot, D.J. Recommended practice for soft ground site characterization: Arthur Casagrande Lecture. In Proceedings of the 12th Panamerican Conference on Soil Mechanics and Geotechnical Engineering, Cambridge, MA, USA, 22–25 June 2003.

63. American Society for Testing and Materials (ASTM). *Annual Book of ASTM Standards, Soil and Rock (I): D420-D5876*; ASTM International: West Conshohocken, PA, USA, 2011.

64. Asociación Española de Normalización y Certificación (AENOR). *Geotecnia: Ensayos de Campo y de Laboratorio*; Asociación Española de Normalización y Certificación (AENOR): Madrid, Spain, 1999.

65. El Howayek, A.; Bobet, A.; Santagata, M. Geologic origin effects on mineralogy, index properties and fabric of a fine-grained carbonatic deposit. *Eng. Geol.* **2017**, *216*, 108–121. [CrossRef]

66. *ASTM D2435-2011*; Standard Test Methods for One-Dimensional Consolidation Properties of Soils Using Incremental Loading. ASTM International: West Conshohocken, PA, USA, 2011.

67. Leroueil, S.; Magnan, J.P.; Tavernas, F. *Embankments on Soft Clays*; Wood, D.M., Translator; Ellis Horwood: New York, NY, USA, 1990.

68. *ASTM D4767-2011*; Standard Test Method for Consolidated Undrained Triaxial Compression Test for Cohesive Soils. ASTM International: West Conshohocken, PA, USA, 2011.

69. Pineda, J.A.; Suwal, L.P.; Kelly, R.B.; Bates, L.; Sloan, W. Characterisation of Ballina clay. *Géotechnique* **2016**, *66*, 556–577. [CrossRef]

70. Dai, F.; Lee, C.F.; Wang, S.; Feng, Y. Stress-strain behaviour of a loosely compacted volcanic-derived soil and its significance to rainfall-induced fill slope failures. *Eng. Geol.* **1999**, *53*, 359–370. [CrossRef]

71. Konkol, J.; Międlarz, K.; Bałachowski, L. Geotechnical characterization of soft soil deposits in Northern Poland. *Eng. Geol.* **2019**, *259*, 105187. [CrossRef]

72. Head, K.H.; Epps, R.J. *Manual of Soil Laboratory Testing, Volume III: Effective Stress Tests*, 3rd ed.; Whittles Publishing: Scotland, UK, 2014.

73. *ASTM D7181-2011*; Standard Test Method for Consolidated Drained Triaxial Compression Test for Soils. ASTM International: West Conshohocken, PA, USA, 2011.

74. Duncan, J.M.; Chang, C.Y. Non-linear analysis of stress and strain in soils. *J. Soil Mech. Found. Div.* **1970**, *96*, 1629–1653. [CrossRef]

75. Wesley, L.D. Influence of structure and composition on residual soils. *J. Geotech. Eng.* **1990**, *116*, 589–603. [CrossRef]

76. Hu, Y.; Lin, P.; Guo, C.; Mei, G. Assessment and calibration of two models for estimation of soil nail loads and system reliability analysis of soil nails against internal failures. *Acta Geotech.* **2020**, *15*, 2941–2968. [CrossRef]

77. Mohamed, M.H.; Ahmed, M.; Mallick, J.; Hoa, P.V. An Experimental Study of a Nailed Soil Slope: Effects of Surcharge Loading and Nails Characteristics. *Appl. Sci.* **2021**, *11*, 4842. [CrossRef]

78. Hong, C.Y.; Liu, Z.X.; Zhang, Y.F.; Zhang, M.X.; Borana, L. Influence of Critical Parameters on the Peak Pullout Resistance of Soil Nails Under Different Testing Conditions. *Int. J. Geosynth. Ground Eng.* **2017**, *3*, 19. [CrossRef]

79. Rocscience. *Slide2, 2D Limit Equilibrium Analysis for Slopes*; Rocscience: Toronto, ON, Canada, 2020.